

Energy Spectra of the Soft X-ray Diffuse Emission in Fourteen Fields Observed with Suzaku

T. YOSHINO^{1*}, K. MITSUDA¹, N. Y. YAMASAKI¹, Y. TAKEI¹, T. HAGIHARA¹, K. MASUI^{1†},
M. BAUER^{1,2‡}, D. MCCAMMON³, R. FUJIMOTO⁴, Q.D. WANG⁵, and Y. YAO^{6,7}

¹*Institute of Space and Astronautical Science, Japan Aerospace Exploration Agency, 3-1-1 Yoshinodai, Sagamihara, 229-8510, Japan*

²*Max-Planck-Institut für extraterrestrische Physik, 85748 Garching, Germany*

³*Department of Physics, University of Wisconsin, Madison, 1150 University Avenue, Madison, WI 53706, USA*

⁴*Department of Physics, Kanazawa University, Kanazawa, 920-1192, Japan*

⁵*Department of Astronomy, University of Massachusetts Amherst, MA 01003, USA*

⁶*Massachusetts Institute of Technology (MIT) Kavli Institute for Astrophysics and Space Research, 70 Vassar Street, Cambridge, MA 02139, USA*

⁷*University of Colorado, CASA, 389 UCB, Boulder, CO 80309, USA*

(Received 2008 December 2; accepted 2009 May 2)

Abstract

The soft diffuse X-ray emission of twelve fields observed with Suzaku are presented together with two additional fields from previous analyses. All have galactic longitudes $65^\circ < \ell < 295^\circ$ to avoid contributions from the very bright diffuse source that extends at least 30° from the Galactic center. The surface brightnesses of the Suzaku nine fields for which apparently uncontaminated ROSAT All Sky Survey (RASS) were available were statistically consistent with the RASS values, with an upper limit for differences of $17 \times 10^{-6} \text{ c s}^{-1} \text{ amin}^{-2}$ in *R45*-band. The OVII and OVIII intensities are well correlated to each other, and OVII emission shows an intensity floor at $\sim 2 \text{ photons s}^{-1} \text{ cm}^{-2} \text{ str}^{-1}$ (LU). The high-latitude OVIII emission shows a tight correlation with excess of OVII emission above the floor, with (OVIII intensity) = $0.5 \times [(\text{OVII intensity}) - 2 \text{ LU}]$, suggesting that temperatures averaged over different line-of-sight show a narrow distribution around $\sim 0.2 \text{ keV}$. We consider that the offset intensity of OVII arises from the Heliospheric solar wind charge exchange and perhaps from the local hot bubble, and that the excess OVII (2-7 LU) is emission from more distant parts of the Galaxy. The total bolometric luminosity of this galactic emission is estimated to be $4 \times 10^{39} \text{ erg s}^{-1}$, and its characteristic temperature may be related to the virial temperature of the Galaxy.

Key words: Galaxy: disk — Galaxy: halo — X-rays: diffuse background — X-rays: ISM

1. Introduction

The soft X-ray diffuse background below 1 keV is considered to consist of the contribution of faint extragalactic sources and emissions from highly ionized ions, such as CVI, OVII, OVIII, FeXVII, and NeIX, in solar neighborhoods and in our Galaxy. The extragalactic contribution, which we refer to as the Cosmic X-ray Background (CXB) in this paper, is estimated to be about 40 % of emission in the so-called ROSAT *R45* band (McCammon et al. 2002), which is approximately $\sim 0.44 - 1 \text{ keV}$. The emission from highly ionized ions is considered to arise from at least three different origins. Among them, the solar wind charge exchange (SWCX) induced emission from the Heliosphere (Cox 1998; Cravens 2000; Lallement 2004),

and the thermal emission from the hot gas in local hot bubble (LHB) (McCammon & Sanders 1990) are hard to be separated from each other using emission spectra above $\sim 0.4 \text{ keV}$. In this energy range, the sum of the two emission components are approximated by a thin-thermal emission of $kT \sim 0.1 \text{ keV}$ without absorption (Smith et al. 2007; Henley et al. 2007; Galeazzi et al. 2007; Kuntz & Snowden 2008; Masui et al. 2009). The remaining emission is considered to arise from more distant part of the galaxy; mostly above or beyond the bulk of absorption in the Galactic disk. Kuntz & Snowden (2000) called this component the “transabsorption” emission (TAE) and separated it in the ROSAT all sky map utilizing the directional dependence of the absorption column density. They found that the emission spectrum can be described by a two-temperature thermal emission model of temperatures $kT \sim 0.10$ and 0.25 keV . However, because there is no constraint on distance other than absorption, it is hard to constrain the origins conclusively.

New insight has been obtained from combined analyses of the absorption lines observed in the energy spectra of extragalactic objects and emission lines of the same ion

* Present Address is NEC corporation, Nisshin-cho 1-10, Fuchu, 183-8551, Japan.

† Present Address is FUJIFILM Advanced Research Laboratories, Ushijima 577, Kaisei-machi, Ashigara-gun, Kanagawa 258-8577, Japan.

‡ Present Address is Radox Laboratories Ltd., 55 Diamond Road, Crumlin, Co. Antrim, United Kingdom, BT29 4QY.

species observed nearby. Yao et al. (2009) analyzed the absorption spectra of LMC X-3 obtained with the transmission grating (HETG) onboard Chandra, and the emission spectra from the blank fields about 30' away from LMC X-3 observed with the CCD camera (XIS) onboard Suzaku. The joint spectral fit of the data shows the hot gas attributed to the TAE component cannot be isothermal. Instead, a thick Galactic hot gaseous disk whose temperature and density decrease exponentially from the Galactic midplane can consistently explain the observations. They obtained scale heights of 1.4 and 2.8 kpc, and the midplane values of 0.31 keV and $1.4 \times 10^{-3} \text{ cm}^{-3}$ for the temperature and the density, respectively.

A similar result was obtained for the sight line toward Mrk 421, although the X-ray emission is mostly based on the ROSAT All Sky Survey data, thus the emission lines are not resolved spectroscopically (Yao & Wang 2007).

In this paper, we analyze energy spectra of the soft X-ray diffuse emission of twelve different fields observed with Suzaku (Mitsuda et al. 2007) and combine them with Suzaku results of two other fields in literature. By virtue of the good energy response function of the CCD camera (Koyama et al. 2007) and the high sensitivity when combined with the X-ray mirror (Serlemitsos et al. 2007), we clearly detected OVII emission from all the fields, and OVIII emission from most of them.

In this paper we concentrate on the XIS1 data which has much larger effective area below 1 keV than other XIS sensors because it employs backside illuminated CCD. Throughout this paper, we quote single parameter errors at the 90 % confidence level unless otherwise specified.

2. Observations and data reduction

2.1. Observations and standard data screening

In Table 1, we show the observations we used in this paper. The analysis results of the seven data sets, Off Filament (Off-FIL), On Filament (On-FIL), North Ecliptic Pole 1 (NEP1), MBM 12 off cloud (M12off), LMC X-3 Vicinity (LX-3), MBM 12 on cloud (M12on), and Midplane 235 (MP235) have been already published.

The data reduction done by Yao et al. (2009) for LX-3 is consistent with that shown in this section. Since Fujimoto et al. (2007) (NEP1) and Smith et al. (2007) (M12off) used version 0.7 processed data, we re-analyzed the data from the data reduction. The second observation of the North Ecliptic Pole direction (NEP2) was made about a half year after the first NEP observation. The aim points of the two observations are identical, although the roll angle was rotated by about 180° .

The two fields at the bottom of Table 1, M12on and MP235, are special directions compared to other twelve fields. M12on is towards the molecular cloud MBM12 located at ~ 100 pc with a bright Cataclysmic Variable in the field of view behind the cloud, and MP235 is in the galactic plane at $b = 235^\circ$ with a large ($N_{\text{H}} = 9 \times 10^{21} \text{ cm}^{-2}$) galactic absorption. They therefore require spectral models different from those of the other fields in

this paper. The spectral results from these two directions have been already published (Smith et al. 2007; Masui et al. 2009) and were analyzed in the same manner as used in this paper, including the geocoronal SWCX removal. We therefore simply adopt their analysis, although we have updated their fits to M12on with more recent calibration data. For these two fields we will simply show the results in tables and figures and will not show the details of analysis in the text.

In all the observations, the XIS was set to the normal clocking mode and the data format was either 3×3 or 5×5 . The Spaced-raw Charge Injection (SCI) was on for Low latitude 86-21 (LL21) and Low latitude 97+10 (LL10). We used version 2.0 processed Suzaku data. We first cleaned the data using the selection criteria: elevation from sunlit/dark earth rim $> 20/5$ deg, cut off rigidity > 8 GV. We checked the dependency of the 0.4 - 0.7 keV counting rate on the Oxygen column density of the sunlit atmosphere in the line of sight using the MSIS atmosphere model (see Fujimoto et al. 2007; Smith et al. 2007; Miller et al. 2008). We found that the counting rate was constant as a function of the column density for the cleaned data. Thus there is no significant neutral O emission from Earth atmosphere in the filtered data.

2.2. Removal of Point sources

We then constructed an X-ray image in 0.3 to 2 keV energy range. We detected point sources in the 17.8×17.8 field of view for all the data sets except for LL10. We removed a circular region centered at the source position from the further analysis. The radius of the circular region was determined so that the counts from the point source outside the circular region becomes less than 3 % of the diffuse X-ray emission in 0.3 to 1 keV energy range. The sum of contribution of point sources is estimated to be less than 6% of the diffuse emission for all the fields except for LH-1 and LL21. The contributions of the two fields, LH-1 and LL21, are respectively 8 and 12 %. For these fields, we analyzed the point source spectra and used the mirror point spread function to determine their residual contribution in OVII and OVIII. We extracted sum of point-source spectra from the circular source regions and performed model fittings. As the background spectra, we used the spectra extracted from source-free circular regions whose distances from the optical axis of the telescope are equivalent to the source regions, respectively. We estimated the upper limits of OVII and OVIII emission intensities of the source regions with spectral fits, then their contamination to the SXDB spectra. The upper limit of contamination was 0.4 LU for OVII emission for the both fields. It was 0.2 LU and 0.6 LU for OVIII emission for LH-1 and LL10, respectively. For GB1428+4217 (GB) a point source of an intensity of $2.6 \times 10^{-13} \text{ erg s}^{-1} \text{ cm}^{-2}$ in the energy band of 0.3 to 1 keV ($22 \times 10^{-13} \text{ erg s}^{-1} \text{ cm}^{-2}$ in 1 to 10 keV) was detected at the center of the field of view. We removed a circular region of a 5 arc minute radius for this observation. The contribution of the source in the counting rate of the remaining region is estimated to be only 0.2 %.

Table 1. Log of observations, ordered by $|b|$

Data set		Obs ID	Date	Exposure (ks)		Aim point	
ID	Field Name (Short Name)			Total	Cleaned	(ℓ, b)	$(E_{\text{Lon}}, E_{\text{Lat}})^*$
1	GB1428+4217 (GB)	701092010	Jun 12-13, 2006	48.7	34.9	(75.9, 64.9)	(194.2, 52.7)
2	High latitude B (HL-B)	500027020	Feb 17-20, 2006	103.6	29.7	(272.4, -58.3)	(4.4, -61.4)
3	Lockman hole 2 (LH-2)	101002010	May 17-19, 2006	80.4	40.0	(149.7, 53.2)	(137.1, 45.1)
4	Lockman hole 1 (LH-1)	100046010	Nov 14-15, 2005	77.0	61.7	(149.0, 53.2)	(137.2, 45.5)
5	Off Filament ^a (Off-FIL)	501001010	Mar 1-2, 2006	80.1	59.6	(278.7, -47.1)	(354.8, -72.6)
6	On Filament ^a (On-FIL)	501002010	Mar 3-6, 2006	101.4	59.2	(278.7, -45.3)	(354.1, -74.4)
7	High latitude A (HL-A)	500027010	Feb 14-15, 2006	73.6	53.2	(68.4, 44.4)	(228.8, 63.5)
8	MBM12 off cloud ^b (M12off)	501104010	Feb 6-8, 2006	75.3	51.0	(157.3, -36.8)	(44.5, 2.3)
9	LMC X-3 Vicinity ^c (LX-3)	500031010	Mar 17-18, 2006	82.0	56.1	(273.4, -32.6)	(41.2, -86.2)
10	North Ecliptic Pole 1 ^d (NEP1)	100018010	Sep 2-4, 2005	106.2	58.7	(95.8, 28.7)	(334.8, 88.7)
11	North Ecliptic Pole 2 (NEP2)	500026010	Feb 10-12, 2006	75.6	16.5	(95.8, 28.7)	(334.8, 88.7)
12	Low latitude 86-21 (LL21)	502047010	May 9-10, 2007	81.5	57.0	(86.0, -20.8)	(347.6, 38.4)
13	Low latitude 97+10 (LL10)	503075010	Apr 15-16, 2008	79.8	40.8	(96.6, 10.4)	(0.7, 70.6)
R1	MBM12 on cloud ^{b,e} (M12on)	500015010	Feb 3-6, 2006	102.9	68.0	(159.2, -34.5)	(47.2, 2.6)
R2	Midplane 235 ^e (MP235)	502021010	Apr 22-25, 2007	189.5	53.0	(235.0, 0.0)	(119.5, -40.6)

Results previously published by ^a Henley et al. (2007), ^b Smith et al. (2007), ^c Yao et al. (2009), ^d Fujimoto et al. (2007), ^e Masui et al. (2009).

* Ecliptic coordinate

2.3. Removal of geocoronal SWCX

The spectrum below 1 keV could be contaminated by the SWCX induced emission from the geocorona (e.g. Cravens et al. (2001)). Fujimoto et al. (2007) reported a flare-like increase of X-ray flux during the Suzaku observation of NEP1, which was clearly visible in the light curve of 256 s time bins. In all other observations, the increase is too small to be recognized in the light curve of 256 or 512 s time bins, but still it could be statistically significant in the X-ray spectra when they are integrated over a certain amount of time (e.g. $\gtrsim 30$ ks). Thus as the last stage of the data reduction, we removed time intervals in which the data can be contaminated by the SWCX from the geocorona.

We consider two parameters which are related to Suzaku's geocoronal SWCX intensity. The first one is the solar wind flux near the Earth. We calculated the solar-wind proton flux at the Earth using ACE SWEPAM data¹. When the ACE SWEPAM data are not available, we used WIND SWE data² or OMNI data from CDAWeb (Coordinated Data Analysis Web)³.

The second parameter is the Earth-center to magnetopause (ETM) distance, where the magnetopause is defined as the lowest position along the sight line of Suzaku where geomagnetic field is open to interplanetary space. The ETM distance is in the range of ~ 2 to ~ 10 Earth radii (R_E), while Suzaku is in a low earth orbit of an about 650 km altitude. Thus it is always looking at the sky through the magnetopause. The probability of a contamination in Suzaku spectra by the SWCX from the geocorona increases if the shortest Earth-center to magnetopause (ETM) distance is $\lesssim 5 R_E$ (Fujimoto et al. 2007). We calculated the ETM distance every 256 s for all the observation periods using the T96 magnetic field

model (Tsyganenko & Sitnov 2005). We obtained the interplanetary plasma parameters required for the calculations from the CDAWeb.

When the sun is quiet the solar wind proton flux stays in the range of $(1-4) \times 10^8$ protons $\text{s}^{-1} \text{cm}^{-2}$, and shows slow (times scales of ~ 10 ks) time variations. On the other hand, during flaring events, it increases and can go up to $\sim 5 \times 10^9$ protons $\text{s}^{-1} \text{cm}^{-2}$, and shows fast ($\lesssim 1$ ks) time variations.

For the four observations, GB1428+4217 (GB), Lockman hole 1 (LH-1), On Filament (On-FIL) and Low latitude 86-21(LL21), the proton flux was always below 4×10^8 protons $\text{s}^{-1} \text{cm}^{-2}$. Among them, during GB and On-FIL observations, the proton flux showed slow variation and the data sets can be divided into two subsets of $(1-2) \times 10^9$ protons $\text{s}^{-1} \text{cm}^{-2}$ and $(2-3) \times 10^9$ protons $\text{s}^{-1} \text{cm}^{-2}$ for GB, and of $(2-3) \times 10^9$ protons $\text{s}^{-1} \text{cm}^{-2}$ and $(3-4) \times 10^9$ protons $\text{s}^{-1} \text{cm}^{-2}$ for On-FIL, respectively. Both during the GB and On-FIL observations, the ETM distance varied in 2 to 10 R_E range. We created spectra for the subsets and performed spectral fits to determine the OVII and OVIII emission intensities. The fitting model used in this analysis will be described in detail in the next section (3.1). We found the difference in the OVII line intensities was less than 2σ for both fields. This corresponds to 1.7 LU and 1.3 LU for GB and On-FIL, respectively. For OVIII, the difference was within 1σ , which is 0.5 and 0.6 LU for GB and On-FIL, respectively.

Among all other observations, in part of HL-B, HL-B, and LH-2 observations, the proton flux stayed below 4×10^8 protons $\text{s}^{-1} \text{cm}^{-2}$, and showed variations of more than 1×10^8 protons $\text{s}^{-1} \text{cm}^{-2}$ was observed. We thus also subdivided the data sets according to the proton flux. We found that the variations of OVII and OVIII intensities were within 2σ level for all those data sets. We thus conclude that when the proton flux is $< 4 \times 10^8$ protons $\text{s}^{-1} \text{cm}^{-2}$ the contamination of geocoro-

¹ The data available at <http://www.srl.caltech.edu/ACE/ACS/>

² The data available at <http://web.mit.edu/afs/athena/org/s/space/www/wind.html>

³ The data available at http://cdaweb.gsfc.nasa.gov/cdaweb/sp_phys/

nal SWCX is relatively small, although there still could remain possibility of contamination of ~ 1.5 LU and ~ 0.5 LU levels for OVII and OVIII, respectively. We thus decided to use all the data for the four observations, (GB, LH-1, On-FIL), and LL21,

For the seven observations, High latitude B (HL-B), Lockman hole 2 (LH-2), Off Filament (Off-FIL), LMC X-3 Vicinity (LX-3), North Ecliptic Pole (NEP1), the second North Ecliptic Pole observation (NEP2) and Low latitude 97+10 (LL10), the proton flux shows flare-like increase and exceeds 4×10^8 protons $\text{s}^{-1} \text{cm}^{-2}$ in about a half of the observation. We thus subdivided those data into two subsets according to the proton flux, and determined the OVII and OVIII intensities. We found significant (more than 2σ in OVII or OVIII) difference between the two spectra for four cases: HL-B, LH-2, NEP1 and NEP2. An example of spectral comparisons is shown in Figure 1. For these four data sets, we decided to use only the time intervals in which the proton flux was lower than 4×10^8 protons $\text{s}^{-1} \text{cm}^{-2}$. These results are consistent with the geocoronal SWCX contamination reported for Suzaku observations of 4U1830-303 vicinities (Mitsuda et al. 2008).

In order to find out why no difference was found in the remaining three observations, we checked the ETM distance of these observations. As already reported in Yao et al. (2009), the ETM distance became as short as $1.4R_E$ during the LX-3 observation. However, the magnetic field was open to anti-sun direction when the ETM distance was $< 5R_E$ during which solar-wind particles cannot penetrate. This explains why there was no significant difference between the high and low proton-flux spectra for this data set. We thus decided to adopt all the data for this observation. During the LL10 and Off-FIL observation, the magnetic field was occasionally open to sun side when the ETM distance dropped below $5R_E$. We decided to simply discard the time intervals with high proton fluxes for these data because we still have enough statistics.

There remain two data sets, High latitude A (HL-A) and MBM12 off cloud (M12off). During the HL-A observation, the proton flux varied in the range of $3 - 6 \times 10^8$ protons $\text{s}^{-1} \text{cm}^{-2}$ but the time interval exceeding 4×10^8 protons $\text{s}^{-1} \text{cm}^{-2}$ was short ($\sim 1/8$ of data). During the M12off observation, it stayed at a level of $\sim 5 \times 10^8$ protons $\text{s}^{-1} \text{cm}^{-2}$. Thus for these data sets, we can not compare spectra with low and high proton fluxes. For HL-A, we subdivided the data sets according to the ETM distance and created two energy spectra with ETM distances = $5 - 10R_E$ and $> 10R_E$. We found that the two spectra with different ETM distances show no significant difference. Thus we will use data with the ETM distances $> 5R_E$. There was a small fraction of the data with the ETM distance $< 5R_E$, which we decided to discard. For M12off, the ETM distance stayed in $7 - 9R_E$. Thus further subdivision was not possible, and we decided to use all the data.

We tried to exclude time intervals for which contamination of time variable geocoronal SWCX was significant. However we should keep in mind that there is still un-

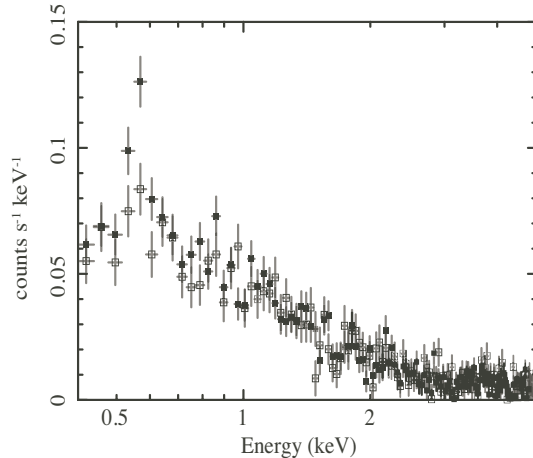


Fig. 1. Energy spectra of High Latitude B (HL-B) for the time intervals with solar wind proton flux higher (filled squares) or lower (open squares) than 4×10^8 protons $\text{s}^{-1} \text{cm}^{-2}$. The vertical error bars are the $1 - \sigma$ statistical errors. The non X-ray background was subtracted. There are large ($> 3 \sigma$) discrepancies between the OVII emission (~ 0.56 keV) intensities of two spectra, which indicates significant geocoronal SWCX contamination in the higher proton-flux data.

certainty of contamination by geocoronal SWCX at 1.5 LU and 0.5 LU levels for OVII and OVIII, respectively. In addition, the last data set, M12off, could have larger contamination. In Table 2, we summarize the process we applied to remove time intervals which are suspected to be contaminated by the SWCX from the geocorona. We also show the process for M12on and MP235 fields in the table.

2.4. Non X-ray background

The non X-ray background (NXB) spectrum was constructed from the dark Earth database using the standard method in which the cut off rigidity distributions of the on-source and the background data were made identical (Tawa et al. 2008). We found 5 to 10 % discrepancies in the counting rates above 10 keV between the NXB and the observation data, suggesting background uncertainty of this level. We also analyzed front-illuminated CCD data (XIS0, XIS2, and XIS3. but XIS2 was not available after November 9, 2006) to determine the intensity of the Cosmic X-ray Background (CXB) above 2 keV for each

Table 2. Summary of Geocoronal SWCX removal process

ID	(1)	(2)	(3)	(4)	(5)	(6)
1 (GB)	✓					
2 (HL-B)		✓				
3 (LH-2)		✓				
4 (LH-1)	✓					
5 (Off-FIL)				✓		
6 (On-FIL)	✓					
7 (HL-A)						✓
8 (M12off)						✓
9 (LX-3)			✓			
10 (NEP1)		✓				
11 (NEP2)		✓				
12 (LL21)	✓					
13 (LL10)				✓		
R1 (M12on)						✓
R2 (MP235)		✓				

(1) The solar wind flux was always $< 4 \times 10^8$ protons $\text{s}^{-1} \text{cm}^{-2}$. All time intervals were adopted.

(2) Excess in the high-solar-wind-flux spectrum. Time intervals with high solar wind flux were discarded.

(3) The geomagnetic field was open to the anti-sun side, when the ETM distance was low ($< 5R_E$). All time intervals were adopted.

(4) The geomagnetic field was occasionally open to the sun side when the ETM distance was low. Time intervals with high solar wind flux were discarded.

(5) Proton flux stayed in $3-6 \times 10^8$ protons $\text{s}^{-1} \text{cm}^{-2}$. Time intervals with ETM distance $< 5R_E$ were discarded.

(6) Proton flux stayed in $3-7 \times 10^8$ protons $\text{s}^{-1} \text{cm}^{-2}$. ETM distance was always $> 10R_E$. All time intervals were used.

sensors. We determined the CXB intensity by the spectral fits. The model function will be described in section 3. The intensities determined by different sensors were consistent with each other within the 90% statistical errors for all observations except for NEP2. For this observation, the intensity from XIS1 were not consistent with those from other three sensors. It was necessary to adjust the NXB level by about 30% for XIS1 to obtain consistent result. This suggests that not only the NXB level but also its spectral shape may vary from the one extracted from the standard NXB data base. The CXB intensity of NEP2 after the NXB correction was consistent with the CXB intensity estimated from NEP1 data. Since in the energy range below 1 keV, the non X-ray background is only about 10 % of the diffuse X-ray background, the spectral parameters derived in section 3 are not sensitive to this level of background uncertainty.

In Suzaku NXB non-subtracted energy spectra, there are three instrumental lines at 1.486, 1.740, and 2.123 keV (Tawa et al. 2008). Since the line intensity and the line spread function of the detector vary with time, the residuals of those lines appears in the NXB subtracted spectra as lines or line-like structures in the 1.3 to 2.1 keV range. In order to study those features in our spectra, we first fitted all the NXB subtracted spectra in the energy range

1.1 to 5 keV. We employed a power-law function absorbed with a Galactic absorption for the continuum and narrow Gaussian functions for the NXB lines. We found that we need to include a line at 1.828 keV for HL-B, and a line at 2.157 keV for LL10 to obtain an acceptable fit. For other data sets, such a line was not required. In the further spectral fits, we include these Gaussian functions with the parameters fixed at the best fit values for these two data sets. The results of the further analysis do not depend on inclusion or non-inclusion of these lines in the models of spectral fits.

2.5. Arf and rmf files

In order to perform spectral fitting, we generated an efficiency file (arf file) for a spatially uniform emission, using the xissimarfgen software version 2008-04-05 (Ishisaki et al. 2007), assuming a 20'-radius flat field as the input emission of the generator. A pulse height re-distribution matrix (rmf file) was created by the script xisrmfgen version 2007-05-14. The calibration files, ae_xi1_quanteff_20070402.fits, ae_xi1_rmffparam_20080311.fits, ae_xi1_makepi_20080131.fits, and ae_xi1_contami_20071224.fits were used to generate the arf and rmf files.

2.6. Contamination of the optical blocking filter

The degradation of low energy efficiency due to the contamination on the XIS optical blocking filter was included in the arf file. The gradient of the contaminant thickness over the optical blocking filter is also taken into account. Systematic errors in the contaminant thickness are estimated to be about 10 % (The Suzaku Technical Description⁴, see also Fujimoto et al. (2007) for early data and Yamasaki et al. (2009) for recent data). We performed all the analysis described in the next section not only for the nominal contaminant thicknesses but also assuming 10% thicker and thinner contaminants. Because the contaminant thickness is gradually increasing with time, we created the arf files of 10% thicker or thinner contaminants by shifting the observation dates from the real dates, except for the 10 % thicker cases of LL21 and LL10. For the two cases, the +10 % thickness is larger than that of the most recent date in the latest calibration database. We thus added an absorption model in the model spectra to represent the extra contamination. For all data sets, we found that the best-fit parameters changed by only small amount when we varied the assumed contamination thickness by ± 10 %. Among the parameters, the OVII emission intensity is most sensitive to the contaminant thickness. The OVII emission intensity varied at most by 0.8 LU (LU = photons s⁻¹cm⁻²str⁻¹), while the statistical errors were 0.5 to 1.5 LU. Thus we will show only the results with nominal contamination thickness.

3. Analysis and results

3.1. Determination of OVII and OVIII emission intensities

In Figure 2, the energy spectra of thirteen data sets are shown, together with the reference data set, M12on. (The spectrum of MP235 is shown in Figure 5). We can clearly see the OVII (~ 0.56 keV) emission lines in all of the spectra.

We first fitted the spectra in 0.4-5.0 keV with a model function, consisting of the CXB component represented by a power-law function or broken power-law functions absorbed with Galactic neutral medium, and two thin thermal-emission components which we consider to represent the Heliospheric SWCX induced emission plus the thermal emission from the local hot bubble, and the thermal emission from more distant part of the Galaxy. As the thin thermal emission model, we used APEC (<http://hea-www.harvard.edu/APEC/>). The first APEC component representing the sum of the SWCX from the Heliosphere and the emission from the local hot bubble (hereafter SWCX+LHB) is unaffected by the Galactic absorption. The contribution of the LHB is considered to be at most one third of this component and could be as small as $\sim 1/20$ (see the discussion by Smith et al. (2007)). The SWCX induced X-ray emission is a non-thermal process. Thus there is no logical reason that the spectrum of this component can be approximated by thermal emis-

sion. In particular, fine structure of lines and line intensity ratios of different transitions must be very different from those of thermal emission (e.g. Kharchenko et al. (2003)). However, the spectrum of this component has been successfully represented by thin thermal models. Since Suzaku does not have enough energy resolution to resolve fine structures of lines, and since this component mainly contributes to the Suzaku spectra of the energy range below ~ 0.6 keV, the same approximation can be applied to the present data.

Galactic emission beyond the LHB may arise inside the bulk of Galactic absorption. However, we assume that the second thermal component is subject to the total Galactic absorption; i.e. the transabsorption emission (TAE). This assumption is consistent with the discussion in the next subsection (3.2). We fixed the column densities of absorption, N_{H} , for the CXB and the TAE components to the total H column density determined by 21cm observations (Dickey & Lockman 1990) except for On Filament (On-FIL) and Off Filament (Off-FIL) data. For these two data sets, Henley et al. (2007) and Henley & Shelton (2008) used the column densities estimated from the 100- μm intensity from the all-sky IRAS maps using the conversion relation for the southern Galactic hemisphere by Snowden et al. (2000). We thus tried spectral fits using two different N_{H} values.

The average AGN spectrum below ~ 1 keV becomes steeper than above ~ 1 keV, and the average photon index was determined to be 1.96 below ~ 1 keV by Hasinger et al. (1996). We thus tried two different models for the CXB: a power-law model with a photon index fixed to 1.4, and a double broken power-law model used by Smith et al. (2007). The latter model consists of two broken power-law functions with photon indices of 1.54 and 1.96 below 1.2 keV and a photon index of 1.4 above the energy. We fixed the normalization of the broken power law component with a low-energy photon index of 1.54 to 5.7 photons s⁻¹ keV⁻¹ str⁻¹ at 1keV and set the normalization of the other broken power-law component free.

First we fixed the elemental abundances of both thin thermal components to the solar value (Anders & Grevesse 1989), and set the temperature and normalization free. We call these models with the double broken power-law CXB model and with the simple power-law CXB model respectively model 1 and model 1'.

In Tables 3 and 4, we summarize the results of the spectral fits. The best fit model functions convolved with the instrument response functions are plotted in Figure 2 for fits with model 1. For HL-B and HL-A with model 1, and for GB and HL-B for model 1', the temperatures of the two thermal components could not be constrained well because of strong coupling between the two components. In these cases, we fixed the temperature of the SWCX+LHB components to the average values of other spectra. For GB and LH-2 with model 1, the existence of the TAE component was not significant. Thus for these two cases we fixed the temperature of the TAE component to the average value of other spectra other than LL10 (0.264 keV), and estimated the upper limit of the normalization pa-

⁴ available from http://www.astro.isas.jaxa.jp/suzaku/doc/suzaku_tdr

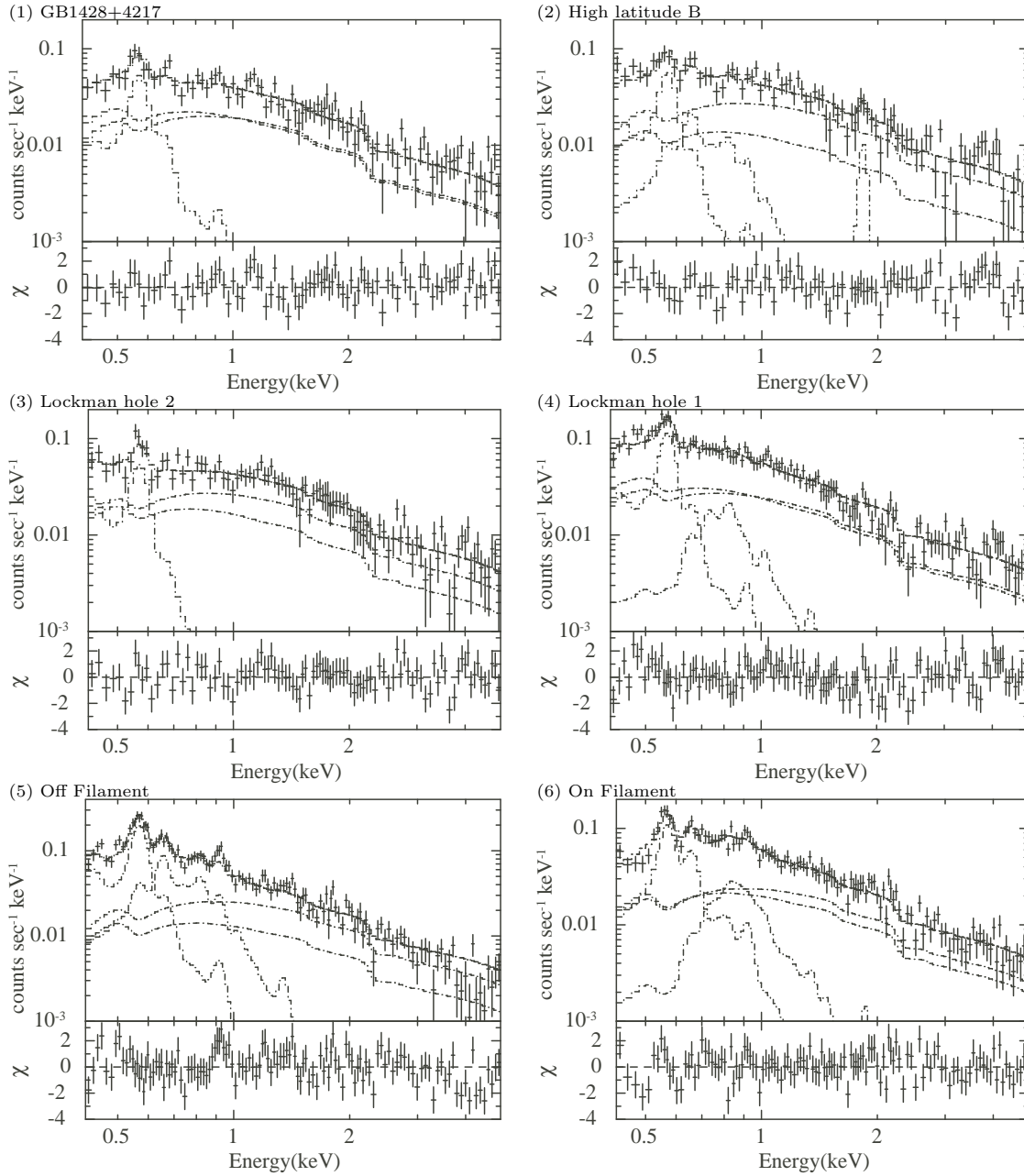


Fig. 2. Observed spectra (crosses) with NXB subtracted, best-fit model 1 and its components (step functions) convolved with the instrument response function and residuals of the fit (bottom panels). The model function consists of three spectral components, CXB, TAE and SWCX+LHB. The TAE and SWCX+LHB were represented by thin thermal emission model of solar abundance. The CXB component was represented by a double broken power-law model. Thus there are two curves for this component. The vertical error bars of data points correspond to the 1σ statistical errors. Some of the spectra show a large excess over the model at Ne K emission (~ 0.9 keV). The hard spectral component which is dominant above ~ 2 keV for M12on represents the Cataclysmic Variable behind the MBM-12 molecular cloud. The observed spectrum of MP235 is found in Figure 5.

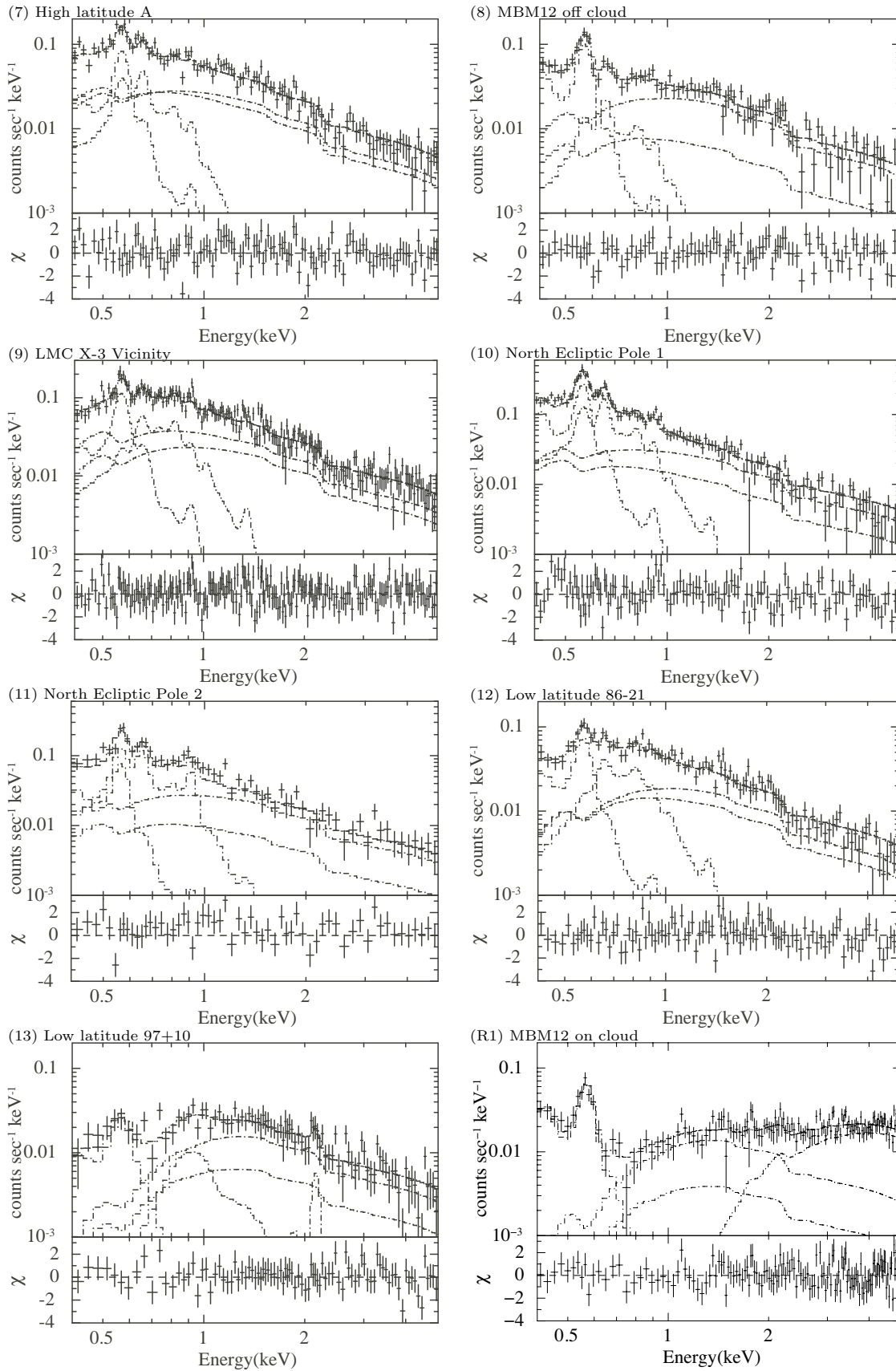


Fig. 2. Continued.

Table 3. Results of three-component (CXB, TAE, SWCX+LHB) spectral fits with the double broken power-law CXB (model 1)

ID	N_{H}^{a}	CXB ^b	TAE		SWCX+LHB		χ^2/dof
	(10^{20}cm^{-2})	Norm ^c	kT (keV)	Norm ^d	kT (keV)	Norm ^d	
1 (GB)	1.40	5.8 ± 0.6	0.264^{e}	$< 1.7^{\text{e}}$	$0.142^{+0.049}_{-0.020}$	6.2 ± 1.4	91.25/92
2 (HL-B)	3.36	2.7 ± 0.6	$0.272^{+0.081}_{-0.076}$	$1.6^{+1.6}_{-0.8}$	0.120^{f}	$6.8^{+1.9}_{-3.6}$	94.45/87
3 (LH-2)	0.56	3.6 ± 0.5	0.264^{e}	$< 1.0^{\text{e}}$	0.099 ± 0.027	$16.3^{+5.4}_{-3.9}$	94.74/99
4 (LH-1)	0.56	$5.6^{+0.4}_{-0.5}$	$0.476^{+0.279}_{-0.149}$	$1.3^{+0.8}_{-0.5}$	$0.137^{+0.011}_{-0.017}$	$8.3^{+3.7}_{-1.4}$	154.08/127
5 (Off-FIL)	4.19	3.0 ± 0.4	$0.271^{+0.018}_{-0.023}$	$7.2^{+1.7}_{-1.0}$	$0.118^{+0.006}_{-0.008}$	$25.5^{+5.5}_{-5.5}$	173.17/122
5' (Off-FIL)	1.90	2.9 ± 0.4	$0.273^{+0.011}_{-0.024}$	$5.8^{+1.4}_{-0.9}$	$0.122^{+0.015}_{-0.009}$	$21.9^{+5.4}_{-5.9}$	169.90/122
6 (On-FIL)	4.61	4.8 ± 0.5	$0.644^{+0.081}_{-0.075}$	$1.9^{+0.5}_{-0.2}$	$0.182^{+0.012}_{-0.013}$	7.0 ± 0.7	128.57/117
6' (On-FIL)	9.60	$5.1^{+0.5}_{-0.6}$	$0.627^{+0.072}_{-0.063}$	$2.7^{+0.6}_{-0.5}$	0.183 ± 0.010	$8.1^{+0.6}_{-0.7}$	127.35/117
7 (HL-A)	1.02	4.9 ± 0.5	$0.237^{+0.045}_{-0.039}$	$3.5^{+1.9}_{-1.1}$	0.120^{f}	$10.0^{+3.2}_{-4.5}$	141.01/116
8 (M12off)	8.74	1.8 ± 0.5	$0.245^{+0.104}_{-0.118}$	$2.4^{+3.4}_{-1.4}$	$0.102^{+0.016}_{-0.080}$	$21.4^{+21.1}_{-6.5}$	86.27/89
9 (LX-3)	4.67	8.7 ± 0.5	$0.310^{+0.087}_{-0.029}$	$6.0^{+1.3}_{-2.5}$	$0.140^{+0.031}_{-0.019}$	$9.9^{+4.1}_{-1.9}$	211.71/196
10 (NEP1)	4.40	$3.0^{+0.5}_{-0.4}$	$0.244^{+0.023}_{-0.017}$	$9.5^{+1.7}_{-1.9}$	$0.113^{+0.009}_{-0.011}$	$23.8^{+6.3}_{-4.1}$	158.44/120
11 (NEP2)	4.40	2.8 ± 0.8	$0.271^{+0.040}_{-0.039}$	$7.7^{+3.1}_{-2.3}$	$0.116^{+0.020}_{-0.025}$	$18.9^{+17.3}_{-8.5}$	60.85/55
12 (LL21)	7.24	4.3 ± 0.5	$0.284^{+0.042}_{-0.035}$	$6.8^{+2.1}_{-1.7}$	$0.109^{+0.019}_{-0.020}$	$24.5^{+27.0}_{-9.6}$	105.03/97
13 (LL10)	27.10	$2.6^{+0.7}_{-0.6}$	$0.738^{+0.243}_{-0.184}$	$1.5^{+0.6}_{-0.7}$	$0.112^{+0.049}_{-0.032}$	$8.1^{+26.2}_{-5.3}$	84.28/ 89
R1 M12on ^g	40.00	1.7 ± 0.6	-	-	$0.095^{+0.014}_{-0.007}$	$18.8^{+8.9}_{-8.0}$	141.62/136
R2 MP235	90.00	6.0 ± 1.0	($0.765^{+0.039}_{-0.041}$	3.73 ± 0.38) ^h	$0.108^{+0.048}_{-0.035}$	$12.4^{+64}_{-7.9}$	75.80/84

^a The absorption column densities for the CXB and TAE components were fixed to the tabulated values. They were estimated from Dickey & Lockman (1990), except for 5' and 6', for which the values were estimated from the 100 μm intensity of the direction (Henley & Shelton 2008).

^b Two broken power-law model was adopted. The photon indices below 1.2 keV were fixed to 1.52 and 1.96. The normalization of the former index component is fixed to $5.7\text{ photons s}^{-1}\text{cm}^{-2}\text{keV}^{-1}\text{str}^{-1}@1\text{keV}$.

^c The normalization of the broken power-law component with a photon index of 1.96 below 1.2 keV.

^d The emission measure integrated over the line of sight, $(1/4\pi)\int n_e n_{\text{H}} ds$ in the unit of $10^{14}\text{cm}^{-5}\text{str}^{-1}$.

^e The TAE component was not significant. The upper limit of the normalization was determined for the average TAE temperature of the TAE component of other observations.

^f Because of the strong coupling between the TAE and LHB+SWCX components, the temperatures of the two components were not well determined. We thus fixed the temperature of the SWCX+LHB component to the average value of other observations.

^g A spectral component for the bright point source represented by an absorbed bremsstrahlung was included in the fits but is not tabulated. The model parameters are $kT = 200\text{ keV}$ (fixed), the normalization factor = $2.66\pm 0.14\times 10^{-12}\text{ cm}^{-5}\text{ str}^{-1}$ (when a point source was replaced with a 20' radius flat emission), and $N_{\text{H}} = 5.5\times 10^{22}\text{cm}^{-2}$ (fixed).

^h This component represents the "narrow bump" component (Masui et al. 2009) rather than the TAE. No absorption was included in this component. This component emits OVIII emissions and the O abundance was set free (the best-fit value is $3.1^{+1.3}_{-1.4}$ solar).

Table 4. Results of three-component (CXB, TAE, SWCX+LHB) spectral fits with the power-law CXB model (model 1')

ID	N_{H}^{a}	CXB ^b	TAE		SWCX+LHB		χ^2/dof
	(10^{20}cm^{-2})	Norm ^c	kT (keV)	Norm ^d	kT (keV)	Norm ^d	
1 (GB)	1.40	10.9 ± 0.6	$0.203^{+0.086}_{-0.050}$	$3.3^{+4.1}_{-1.4}$	0.112^{e}	$8.1^{+6.3}_{-4.7}$	89.86/91
2 (HL-B)	3.36	8.0 ± 0.5	$0.273^{+0.066}_{-0.043}$	$2.3^{+1.0}_{-0.9}$	0.112^{e}	$9.5^{+2.6}_{-2.9}$	96.37/87
3 (LH-2)	0.56	$8.7^{+0.5}_{-0.6}$	$0.335^{+0.160}_{-0.148}$	$1.0^{+1.7}_{-0.6}$	$0.087^{+0.021}_{-0.030}$	$36.4^{+128.5}_{-23.9}$	89.76/97
4 (LH-1)	0.56	$10.6^{+0.4}_{-0.5}$	$0.354^{+0.069}_{-0.038}$	2.5 ± 0.6	$0.116^{+0.013}_{-0.008}$	$15.2^{+4.2}_{-4.1}$	172.90/127
5 (OFF-FIL)	4.19	8.2 ± 0.4	$0.273^{+0.017}_{-0.019}$	$7.9^{+1.5}_{-1.0}$	$0.115^{+0.009}_{-0.006}$	$28.9^{+5.4}_{-5.8}$	178.04/122
5' (OFF-FIL)	1.90	8.2 ± 0.4	$0.276^{+0.012}_{-0.021}$	$6.5^{+1.3}_{-0.9}$	$0.118^{+0.011}_{-0.008}$	$25.7^{+5.8}_{-5.7}$	174.37/122
6 (ON-FIL)	4.61	$10.0^{+0.5}_{-0.4}$	$0.626^{+0.073}_{-0.065}$	2.1 ± 0.5	0.182 ± 0.011	$7.8^{+0.7}_{-0.6}$	124.99/117
6' (ON-FIL)	9.60	10.2 ± 0.5	$0.618^{+0.062}_{-0.056}$	$3.0^{+0.5}_{-0.6}$	$0.183^{+0.010}_{-0.009}$	$8.8^{+0.7}_{-0.6}$	131.00/117
7 (HL-A)	1.02	10.1 ± 0.4	$0.242^{+0.036}_{-0.049}$	$4.9^{+3.0}_{-1.3}$	$0.093^{+0.020}_{-0.046}$	$27.8^{+56.1}_{-13.3}$	142.17/115
8 (M12off)	8.74	7.2 ± 0.4	$0.260^{+0.071}_{-0.069}$	$2.7^{+2.8}_{-1.0}$	$0.101^{+0.015}_{-0.012}$	$23.9^{+10.6}_{-10.6}$	86.99/89
9 (LX-3)	4.67	13.4 ± 0.5	$0.308^{+0.032}_{-0.023}$	$7.6^{+1.2}_{-1.5}$	$0.125^{+0.021}_{-0.013}$	$14.7^{+5.8}_{-4.1}$	214.27/196
10 (NEP1)	4.40	8.1 ± 0.4	$0.250^{+0.023}_{-0.016}$	$9.9^{+1.7}_{-1.8}$	$0.112^{+0.008}_{-0.011}$	$26.8^{+7.7}_{-4.1}$	171.74/120
11 (NEP2)	4.40	8.1 ± 0.7	0.275 ± 0.036	$8.3^{+2.9}_{-1.9}$	$0.113^{+0.024}_{-0.023}$	$21.8^{+19.2}_{-9.0}$	63.15/55
12 (LL21)	7.24	9.5 ± 0.5	$0.287^{+0.033}_{-0.031}$	$7.6^{+1.7}_{-1.5}$	$0.101^{+0.018}_{-0.012}$	$33.5^{+25.7}_{-14.5}$	104.43/97
13 (LL10)	27.10	$7.8^{+0.5}_{-0.6}$	$0.721^{+0.190}_{-0.166}$	$1.9^{+0.8}_{-0.6}$	$0.113^{+0.052}_{-0.030}$	$8.0^{+19.9}_{-5.3}$	84.70/89
R1 M12on ^f	40.00	$7.2^{+0.6}_{-0.5}$	-	-	$0.096^{+0.014}_{-0.007}$	$18.5^{+8.9}_{-7.8}$	141.34/136
R2 MP235	90.0	11.1 ± 0.9	$(0.766^{+0.041}_{-0.039})^{\text{g}}$	$3.75^{+0.40}_{-0.37})^{\text{g}}$	$0.105^{+0.051}_{-0.032}$	$14.1^{+6.4}_{-9.6}$	76.54/84

^a The absorption column densities for the CXB and TAE components were fixed to the tabulated values. They were estimated from Dickey & Lockman (1990), except for 5' and 6'. The column densities were estimated from the $100\ \mu\text{m}$ intensity of the direction.

^b A power-law model with a photon index of 1.4 was adopted.

^c The normalization of the power-law function with the unit of photons $\text{s}^{-1}\text{cm}^{-2}\text{keV}^{-1}\text{str}^{-1}@1\text{keV}$.

^d The emission measure integrated over the line of sight, $(1/4\pi)\int n_e n_{\text{H}} ds$ in the unit of $10^{14}\text{cm}^{-5}\text{str}^{-1}$.

^e Because of the strong coupling between the TAE and LHB+SWCX components, the temperatures of the two components were not well determined. We thus fixed the temperature of the SWCX+LHB component to the average values of other observations.

^f The model parameters for the point source were $kT = 200\text{keV}$ (fixed), the normalization factor = $2.65 \pm 0.14 \times 10^{-12}\text{cm}^{-5}\text{str}^{-1}$ (for a 20' radius flat emission), and $N_{\text{H}} = 5.5 \times 10^{22}\text{cm}^{-2}$ (fixed). See table note (g) of Table 3.

^g "Narrow bump" component. The best-fit O abundance was $3.1^{+1.3}_{-1.2}$. See table note (h) of Table 3.

parameter. Although some different fitting procedures were necessary between models 1 and 1' for a few data sets as described above, the best-fit parameter values of the TAE and SWCX+LHB components determined using different CXB models are consistent within the statistical errors. We performed all the fits shown in this paper using two different CXB models. However, since all of those results are consistent with each other within the statistical errors, we will only show the results with the double broken power-law model for the CXB in the further analysis.

For the On-FIL and Off-FIL results in Tables 3 and 4, we find the best-fit parameters to be consistent with each other within the statistical errors for both absorption values. We performed all the fittings shown later for these data sets with both column densities but continued to find consistent results, and so will show only the results using the absorption column densities from Dickey & Lockman (1990).

The resultant χ^2 values were generally good (reduced χ^2 is $0.95 - 1.42$ for $87 - 196$ degrees of freedom.) The best-fit values of the temperatures of the two thin-thermal models are contained in a relatively narrow ranges. They are

from 0.10 to 0.14 keV for the LHB + SWCX component and from 0.22 and 0.48 keV for the TAE, except for the TAE temperatures of On-FIL ($kT = 0.644\text{keV}$) and LL10 ($kT = 0.738\text{keV}$).

We then estimated the surface brightness of OVII K_{α} and OVIII K_{α} emission. We set the Oxygen abundances of the two APEC models to 0 and added two Gaussian functions that represent OVII K_{α} and OVIII K_{α} emission. We set the intrinsic width of the Gaussian functions to a value small compared to the detector energy resolution. We did not include absorption in the Gaussian components. We set the centroid energies and the normalization parameters of the Gaussians and the normalization parameters of the CXB and APEC components free. We set the intensities of the TAE component to 0 for GB and LH-1, because we had obtained only upper limits for this component. The surface brightness of a line is calculated from the best-fit value of the Gaussian normalization.

The OVII K_{β} emission is at 666 eV which will therefore blend with the OVIII K_{α} emission at 654 eV. We estimated the OVII K_{β} intensity from the best-fit value of Gaussian normalization of OVII K_{α} and subtracted it

Table 5. Results of spectral fits to determine OVII and OVIII line intensities with broken-power-law CXB model (model 1)

ID	CXB ^a	TAE ^{a,b}	SWCX+LHB ^b	OVII		OVIII ^f		χ^2/dof
	Norm ^c	Norm ^d	Norm ^d	Centroid	Norm ^e	Centroid	Norm ^e	
1 (GB)	5.7±0.6	-	4.5 ^{+5.6} _{-4.5}	0.560 ^{+0.010} _{-0.008}	3.6 ^{+0.9} _{-1.0}	0.664 ^{+0.017} _{-0.018}	0.7±0.5	83.19/87
2 (HL-B)	2.4±0.6	1.9 ^{+1.6} _{-1.5}	14.9±5.4	0.560 ^{+0.009} _{-0.010}	2.3±0.7	0.654 ^{+0.010} _{-0.014}	0.9±0.4	80.06/80
3 (LH-2)	3.6±0.5	-	18.3 ^{+9.1} _{-10.1}	0.568 ^{+0.008} _{-0.006}	2.5±0.7	0.654 ^g	< 0.4	93.58/97
4 (LH-1)	5.6±0.5	1.2±0.4	11.8 ^{+3.2} _{-3.3}	0.562 ^{+0.003} _{-0.002}	4.1±0.5	0.659 ^{+0.015} _{-0.017}	0.5±0.3	124.53/ 92
5 (OFF-FIL)	3.0±0.4	9.1±1.3	31.5 ^{+4.5} _{-4.7}	0.566 ^{+0.002} _{-0.004}	9.5±0.7	0.653 ^{+0.004} _{-0.005}	2.5±0.4	154.66/118
6 (ON-FIL)	5.0±0.5	2.1±0.5	4.7 ^{+3.5} _{-3.7}	0.563 ^{+0.004} _{-0.005}	5.2 ^{+1.0} _{-0.6}	0.660 ^{+0.008} _{-0.006}	1.6±0.3	113.18/113
7 (HL-A)	5.0±0.5	4.9±2.1	13.7±4.7	0.564±0.004	4.5±0.6	0.647 ^{+0.007} _{-0.011}	1.6±0.4	134.71/111
8 (M12off)	1.9 ^{+0.4} _{-0.5}	2.9 ^{+2.1} _{-1.9}	24.3 ^{+5.2} _{-5.3}	0.564±0.004	4.4±0.5	0.662 ^{+0.011} _{-0.010}	0.6±0.3	79.05/85
9 (LX-3)	8.8±0.5	7.3 ^{+1.2} _{-1.3}	11.9 ^{+4.1} _{-4.2}	0.570±0.004	6.0±0.7	0.654±0.006	1.8±0.4	206.76/192
10 (NEP1)	3.1 ^{+0.3} _{-0.5}	13.4 ^{+2.0} _{-1.7}	29.1 ^{+3.5} _{-3.4}	0.567 ^{+0.003} _{-0.001}	8.9±0.5	0.653 ^{+0.004} _{-0.002}	2.8 ^{+0.3} _{-0.3}	165.23/116
11 (NEP2)	3.4 ^{+0.8} _{-0.7}	8.2 ^{+2.6} _{-2.7}	25.1 ^{+7.3} _{-7.2}	0.568 ^{+0.006} _{-0.004}	7.0±1.1	0.656 ^{+0.006} _{-0.008}	2.6±0.7	56.20/51
12 (LL21)	4.6±0.5	8.4 ^{+1.7} _{-1.8}	27.3 ^{+7.4} _{-7.5}	0.568 ^{+0.006} _{-0.005}	6.4 ^{+0.8} _{-0.9}	0.652±0.010	1.8±0.5	108.14 /93
13 (LL10)	2.6±0.6	1.7±0.7	10.5±5.6	0.554 ^{+0.019} _{-0.018}	1.7 ^{+1.3} _{-0.7}	0.642 ^{+0.022} _{-0.034}	0.4 ^{+0.3} _{-0.3}	80.63/87
R1 M12on ^h	1.7 ^{+0.5} _{-0.5}	-	20.5 ^{+4.2} _{-3.9}	0.564 ^{+0.005} _{-0.006}	2.9 ± 0.5	0.654 ^g	< 0.4	141.69/135
R2 MP235	6.25 ^{+0.9} _{-1.0}	(4.0 ^{+0.4}) ⁱ	19.5 ^{+7.8} _{-10.5}	0.578 ^{+0.005} _{-0.011}	2.1 ^{+0.8} _{-0.6}	0.673 ^{+0.007} _{-0.024}	0.9±0.3	77.18/83

^a The absorption column densities for the CXB and TAE components were fixed to the values tabulated in Table 3.

^b The temperature of TAE and SWCX+LHB components were fixed to the best fit values tabulated in Table 3.

The O abundance of the both components was set to 0 in the fits.

^c The unit is phtons s⁻¹cm⁻² keV⁻¹str⁻¹@1keV.

^d The emission measure integrated over the line of sight, $(1/4\pi) \int n_e n_H ds$ in the unit of 10¹⁴cm⁻⁵ str⁻¹.

^e The unit is LU =phtons s⁻¹ cm⁻² str⁻¹.

^f Contribution of OVII K_β emission in the Gaussian fitting function is subtracted using K_α intensity (see text).

^g The centroid energy was fixed to obtain the upper limit of the intensity.

^h An additional spectral component was included to represent the point source. See table note (g) of Table 3.

ⁱ "Narrow bump" component. The O abundance of this component was also set to 0. See table note (h) of Table 3.

from the Gaussian normalization of OVIII K_α. The ratio, u , of OVII K_β to OVII K_α intensities is a slow function of the plasma temperature for thermal emission. As we will show later, the temperature of the TAE component determined from O emission is in the range of $kT = 0.19$ to 0.23 keV. Then $u = 0.056$. If the emission is due to SWCX, $u = 0.083$ (Kharchenko et al. 2003). We estimated the OVII K_β intensity assuming that 2 LU of OVIII K_α is from SWCX and the rest from thermal emission of $kT = 0.19$ to 0.23 keV (see below). The difference of the estimation from the totally SWCX or totally thermal cases is at most 0.2 LU, which is smaller than the statistical errors of OVIII intensity.

In Table 5 we summarize the results of the spectral fits. The centroid energy of OVIII had to be fixed to the theoretical value for LH-2, because we obtained only an upper limit for this data set. Except for this case, the centroid energies are consistently determined to be equal to their expected values within the systematic errors of energy scale calibration (5 eV, Koyama et al. 2007, also see the Suzaku Technical Description).

The OVII emission intensities of NEP1 and NEP2 are not consistent with each other within the 90 % statistical errors, while the OVIII emission intensities are consistent.

The difference between the best fit values of OVII is 1.9 LU. In the previous section, we discussed that time variable geocoronal SWCX of 1.5 - 2 LU level can remain in our spectra. Thus, the difference can be partly due to contamination of the geocoronal SWCX. Temporal variations of Heliospheric SWCX could also contribute to the difference.

3.2. Correlation between OVII and OVIII intensities

In Figure 3, we plot the derived OVIII emission intensity as a function of the OVII intensity, and include the data points for M12on and MP235 from Masui et al. (2009). In the figure we notice two remarkable characteristics. First, there is a floor in the OVII intensity at ~ 2 LU. Second, all the data points except for three (HL-B, MP235, and LL10) approximately follow the relation (OVIII intensity) = 0.5 × [(OVII intensity) - 2 LU]. Masui et al. (2009) proposed that the OVIII emission line of the midplane field, MP235, is associated with a ~ 0.8 keV component that may arise from faint young dM stars in the Galactic disk. As we discuss later, the low latitude field at $b = 10^\circ$, LL10, is also considered to contain emission of similar origin. Such high temperature emission produces little OVII. We thus consider that the floor of OVII emission and the strong

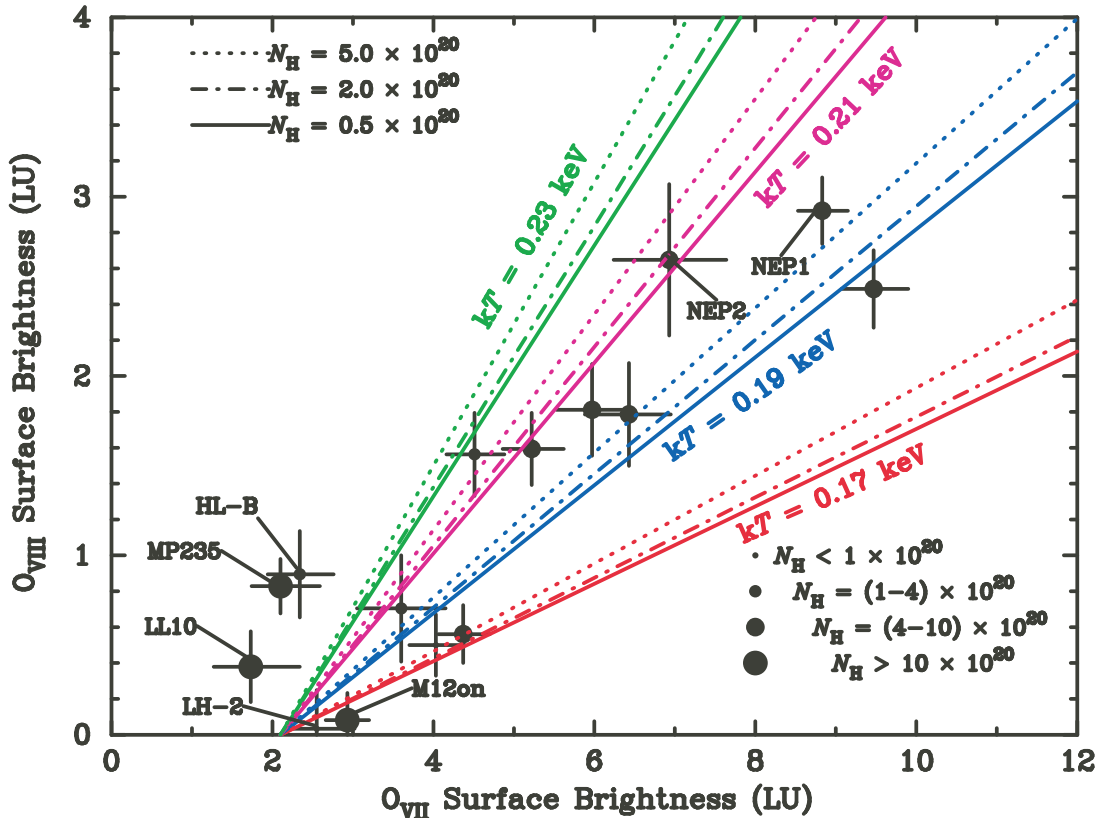


Fig. 3. Relation between OVII and OVIII surface brightnesses for the 14 sky fields observed with Suzaku. The horizontal and vertical bars of data points show the 1σ errors of the estimation. The contribution of OVII $K\beta$ emission in the Gaussian function for OVIII $K\alpha$ is subtracted (see Table 5 and text). The diagonal lines show the relation between OVII and OVIII, assuming an offset OVII emission of 2.1 LU and emission from a hot plasma of the temperature and the absorption column density shown in the figure. The Galactic absorption column density of the observation fields are indicated by the maker size of the data points. The short names of five data points on the intensity floor of OVII emission are also shown.

correlation between additional OVII and OVIII intensities suggest that the OVII emission consists of two emission components of different origins; an emission component which emits OVII of ~ 2 LU and no or weak OVIII emission (the floor component), and the other component which emits OVII of ~ 0 to ~ 7 LU and the OVIII intensity is about a half of OVII (the linear component).

Taking into account possible systematic error of OVII intensity due geocoronal SWCX (~ 1.5 LU), M12on and LH-2 are also on the floor. The OVII emission of the M12on field must arise from the near side of the MBM-12 molecular cloud whose distance is 60 - 300 pc. Assuming the midplane space-averaged neutral density (Ferrière 2001), the absorption length of OVII emission is estimated to be 300 pc for MP235. The total Galactic absorption column density of LL10 ($|b| = 10^\circ$) is $2.7 \times 10^{21} \text{ cm}^{-2}$, through which only 10 % of OVII photons can penetrate. These indicate that the floor component is "local" emission and is associated with the SWCX + LHB component of the spectral model (see also discussion in the first paragraph of section 4.2). The emission temperature of the SWCX + LHB component is $kT \sim 0.1$ keV when it is described with thermal emission. This is consistent with the weak OVIII emission of the floor component.

Then the linear component is likely to arise from more distant part of our Galaxy. It is remarkable that LL21 ($|b| = 20^\circ$) contains significant linear component ($6.4 - 2 = 4.4$ LU), even though the low Galactic latitude. The absorption column density of this direction, $7.2 \times 10^{20} \text{ cm}^{-2}$, is about quarter of LL10 column density and the transmission of the OVII emission is about 54 %. This suggests that a large fraction of the linear component arises from beyond the bulk of Galactic absorption, although the possibility that the difference between LL10 and LL21 is mainly due to spatial fluctuation of the emission measure cannot be ruled out. We thus consider that the linear component is associated with the TAE component. This component emits OVII and OVIII with an intensity ratio of about 2 to 1 and shows field-to-field variations of ~ 0 to ~ 7 LU in OVII intensity. The lines in Figure 3 show OVII - OVIII intensity relations for different temperatures and absorption column densities. We have assumed 2.1 LU as the OVII floor intensity, using the value for the midplane field (MP235). The lines suggest that the average temperatures along each line of sight of the plasmas emitting the OVIII emission and the OVII emission above the floor are in a relatively narrow range of $kT \sim 0.19$ to 0.23 keV if they are arising from collisionally equilibrium plasma

in spite of the large OVII intensity variations (~ 0 to ~ 7 LU).

In Figure 4, we plotted the OVII and OVIII emission intensities as functions of absolute Galactic latitude $|b|$ (a), and as a function of absolute ecliptic latitude (b). The two data points marked with an open circle are M12on and MP235. The correlations of OVII and OVIII emission intensities to Galactic latitude and ecliptic latitude are not very clear. Near solar minimum, Heliospheric SWCX emission is expected to be enhanced in low ecliptic latitude region of $\lesssim 20^\circ$ by ~ 1.5 LU (Koutroumpa et al. 2006). Such small difference may be masked by the spatial variations of the TAE, systematic errors in geocoronal-SWCX removal, and time variations of Heliospheric SWCX. The relevance of Galactic latitude (for TAE) and ecliptic latitude (for SWCX emission) are discussed in sections 4.2 and 4.1, respectively.

3.3. Spectral models consistently describe O emission

If the OVII emission originates in the two plasma emission components of the model as discussed above, we would expect approximately constant temperature and normalization for the SWCX+LHB component that provides the floor to the Ovii rate and a constant temperature ($kT \sim 0.2$ keV) for the TAE component with its constant OVIII/OVII ratio. However, the results of the spectral fits shown in Table 3 (and Table 4 do not show such tendency. The Ovii emission intensities of the SWCX+LHB component estimated using the best-fit parameters in Table 3 vary from 2 to 5.5 LU. The temperature of the TAE component is significantly higher than 0.2 keV and is far from constant.

We consider that this discrepancy is related to the Fe and Ne emission. When we fixed the abundances (Fe to O, and Ne to O ratios) of the hot gas in the spectral fits, the temperature of the TAE component was mostly determined by Fe-L and/or Ne-K emission rather than O emission. Then the temperature and the intensity of the SWCX+LHB component was optimized to fill the remaining emission. We notice relatively large residual near Ne K emission energy, in some of the residual plots in Figure 2. We will now try fixing the temperature and the normalization of the SWCX+LHB component, and allowing the Ne and Fe abundances of the TAE component to vary to see if we can still get good fits and if the temperatures of the second component will be closer to 0.2 keV. This is model 2.

As discussed in the previous subsection, the OVII emission from the three fields, M12on, MP235, and LL10 contains only the SWCX+LHB component. The temperature and normalization (emission measure) derived for that component (see Tables 3 and 4) are, respectively, about 0.11 keV and $14 \times 10^{14} \text{cm}^{-5} \text{str}^{-1}$ for all three fields, which is consistent with the parameters obtained for model fitting of data from the LMC X-3 vicinity (LX-3) by Yao et al. (2009) (0.103 keV and $18.4 \times 10^{14} \text{cm}^{-5} \text{str}^{-1}$), which were derived from previous XMM-Newton and Suzaku observations of directions with absorption gas. For the model 2 spectral fits, we therefore adopted the best fit

value of the midplane observation (Table 3) as representative of SWCX+LHB parameters.

In Table 6 and Figure 5 we show the results of the fits. The χ^2 values are generally good with the reduced χ^2 values in the range of 0.95 – 1.28 for the degrees of freedom of 91 – 196, although most of them are larger than those for the fit with the first model in Table 3. For five of the spectra, the abundances were not constrained well. We thus fixed the Fe and Ne abundances to the solar value. For LH-2, the existence of the TAE was not significant. We estimated the upper limit of the intensity fixing the temperature to the average value of the other spectra. Excluding HL-B and LL10, the temperature of the TAE component are in the range of 0.18 to 0.24 keV with an average of 0.22 keV, which is significantly lower than the temperatures obtained by model 1.

In model 2, the strong Fe-L and Ne K lines are explained by over-abundance of those elements. In particular, $\sim 3 \times$ solar abundance was required for Ne for four fields. We consider that the strong Ne and Fe emissions could be also represented by a higher temperature emission component with solar abundances. For model 3, we fixed the temperature and the abundance of the TAE component to the average of model 2 (0.222 keV) and to the solar value, respectively. We introduce a fourth emission component with higher temperature which we denote TAE'. In Table 7, we show the results for the four fields. The resultant χ^2 values are comparable to those for model 2. In model 3, the excess Ne and Fe emissions are explained by emission with a temperature in the range of 0.6 to 0.9 keV, and an emission measure of $(1-2) \times 10^{14} \text{cm}^{-5} \text{str}^{-1}$.

4. Discussion

4.1. Heliospheric Solar wind charge exchange

Although we have been careful to avoid possible contamination by geocoronal SWCX through the selection procedures discussed in section 2, contributions from SWCX in interplanetary space are at best only partially removed by these methods since the long transit times through the solar system wash out the very large short-term intensity variations seen by monitor satellites located in the ecliptic plane near the Earth. Models of this heliospheric SWCX emission are highly uncertain, but some predict that a large fraction of the Galactic R_{45} emission is from this source (Koutroumpa et al. 2006; Koutroumpa et al. 2008), making it one of the most severe limitations in determining the true interstellar and halo contributions.

Solar activity affects the solar wind densities and ionization temperature. Near the solar maximum, the slow solar winds which have high ionization temperatures and high densities are ejected from the sun resulting in stronger SWCX induced OVII and OVIII emissions (Koutroumpa et al. 2006) than in solar minimum. Near the solar minimum, slow solar winds are emitted from the equator region of the sun, and high speed, low-density, low-ionization-temperature winds are emitted from the high latitude region of the sun. Discrepancies between early XMM-Newton or Chandra observations which were also made

Table 6. Results of three-component (CXB, TAE, SWCX+LHB) spectral fit with SWCX+LHB temperature and normalization fixed, and with double broken power law CXB (model 2)

ID	N_{H}^{a}	CXB ^b		TAE			χ^2/dof
	10^{20}cm^{-2}	Norm ^c	kT (keV)	Ne	Fe	Norm ^d	
1 (GB)	1.40	$5.6^{+0.7}_{-0.7}$	$0.222^{+0.111}_{-0.068}$	1^{e}	1^{e}	$1.2^{+1.0}_{-1.0}$	95.12/ 92
2 (HL-B)	3.36	$2.5^{+0.5}_{-0.6}$	$0.296^{+0.093}_{-0.049}$	1^{e}	1^{e}	$1.6^{+0.9}_{-0.7}$	95.14/88
3 (LH-2)	0.56	$3.5^{+0.4}_{-0.5}$	0.222	1^{e}	1^{e}	< 0.7	95.33/100
4 (LH-1)	0.56	$5.6^{+0.5}_{-0.5}$	$0.237^{+0.262}_{-0.058}$	$3.79^{+6.43}_{-2.02}$	$2.49^{+13.60}_{-1.98}$	$2.0^{+0.6}_{-0.6}$	162.31/127
5 (OFF-FIL)	4.19	$3.1^{+0.4}_{-0.4}$	$0.181^{+0.008}_{-0.008}$	$3.53^{+1.01}_{-0.80}$	$2.99^{+2.75}_{-1.21}$	$15.3^{+1.1}_{-1.1}$	159.33/122
6 (ON-FIL)	4.61	$5.0^{+0.5}_{-0.5}$	$0.239^{+0.027}_{-0.025}$	$3.46^{+1.91}_{-1.19}$	$1.88^{+1.97}_{-0.85}$	$5.2^{+0.9}_{-0.9}$	130.94/117
7 (HL-A)	1.02	$4.9^{+0.5}_{-0.5}$	$0.243^{+0.031}_{-0.032}$	$0.91^{+1.06}_{-0.78}$	$0.51^{+1.16}_{-0.48}$	$4.3^{+0.8}_{-0.8}$	138.89/115
8 (M12off)	8.74	$2.0^{+0.4}_{-0.4}$	$0.184^{+0.023}_{-0.030}$	1^{e}	1^{e}	$4.9^{+1.2}_{-1.2}$	89.83/91
9 (LX-3)	4.67	$8.8^{+0.5}_{-0.5}$	$0.213^{+0.026}_{-0.018}$	$3.04^{+1.282}_{-1.168}$	$3.12^{+1.978}_{-1.590}$	$7.7^{+1.2}_{-0.5}$	210.94/196
10 (NEP1)	4.40	$3.2^{+0.5}_{-0.4}$	$0.191^{+0.006}_{-0.006}$	$2.09^{+0.53}_{-0.47}$	$1.69^{+0.75}_{-0.55}$	$15.3^{+0.9}_{-0.9}$	164.60/120
11 (NEP2)	4.40	$3.4^{+0.7}_{-0.7}$	$0.206^{+0.041}_{-0.019}$	$2.65^{+1.43}_{-1.34}$	$1.59^{+1.743}_{-1.177}$	$10.8^{+1.8}_{-1.8}$	57.94/55
12 (LL21)	7.24	$4.7^{+0.5}_{-0.5}$	$0.193^{+0.019}_{-0.016}$	$2.00^{+1.15}_{-0.86}$	$2.88^{+3.53}_{-1.33}$	$11.1^{+1.7}_{-1.7}$	112.77/97
13 (LL10)	27.10	$2.5^{+0.7}_{-0.7}$	$0.752^{+0.240}_{-0.177}$	1^{e}	1^{e}	$1.6^{+0.7}_{-0.7}$	91.44/91

^a The absorption column densities for the CXB and TAE components were fixed to the tabulated values.

^b Two broken power-law model was adopted. The photon indexes below 1.2 keV were fixed to 1.52 and 1.96 . The normalization of the former index component is fixed to 5.7, and only the normalization of the other component was allowed to vary.

^c The normalization of one of the broken power-law components with the unit of photons $\text{s}^{-1}\text{cm}^{-2}\text{keV}^{-1}\text{str}^{-1}@1\text{keV}$.

^d The emission measure integrated over the line of sight, $(1/4\pi) \int n_e n_{\text{H}} ds$ in the unit of $10^{14}\text{cm}^{-5}\text{str}^{-1}$.

^e The abundance was not constrained well, thus fixed to the solar value.

Table 7. Results of four-component (CXB, TAE, TAE', SWCX+LHB) spectral fit with SWCX+LHB normalization and temperature , and TAE temperature fixed, and with double broken power law CXB (model 3)

ID	N_{H}^{a}	CXB ^b		TAE		TAE'		χ^2/dof
	10^{20}cm^{-2}	Norm ^c	kT (keV)	Norm ^d	kT (keV)	Norm ^d		
4 (LH-1)	0.56	$5.3^{+0.5}_{-0.6}$	0.222	$1.9^{+0.6}_{-0.6}$	$0.746^{+0.326}_{-0.382}$	$1.0^{+0.4}_{-0.3}$	160.48/128	
5 (Off-FIL)	1.90	$2.6^{+0.5}_{-0.5}$	0.222	$10.3^{+0.7}_{-0.7}$	$0.861^{+0.132}_{-0.115}$	$0.8^{+0.4}_{-0.4}$	197.26/123	
6 (On-FIL)	9.60	$5.1^{+0.5}_{-0.6}$	0.222	$9.0^{+1.1}_{-1.2}$	$0.676^{+0.094}_{-0.090}$	$1.9^{+0.6}_{-0.5}$	122.93/118	
9 (LX-3)	4.67	$8.5^{+0.7}_{-0.6}$	0.222	$7.4^{+1.0}_{-1.1}$	$0.559^{+0.109}_{-0.193}$	$1.8^{+0.4}_{-0.7}$	216.50/197	

^a The absorption column densities for the CXB, TAE, and TAE' components were fixed to the tabulated values.

^b Two broken power-law model was adopted. The photon indexes below 1.2 keV were fixed to 1.52 and 1.96 . The normalization of the former index component is fixed to 5.7, and only the normalization of the other component was allowed to vary.

^c The normalization of one of the broken power-law components with the unit of photons $\text{s}^{-1}\text{cm}^{-2}\text{keV}^{-1}\text{str}^{-1}@1\text{keV}$. Add 5.7 to obtain the total flux at 1 keV.

^d The emission measure integrated over the line of sight, i.e. $(1/4\pi) \int n_e n_{\text{H}} ds$ in the unit of $10^{14}\text{cm}^{-5}\text{str}^{-1}$.

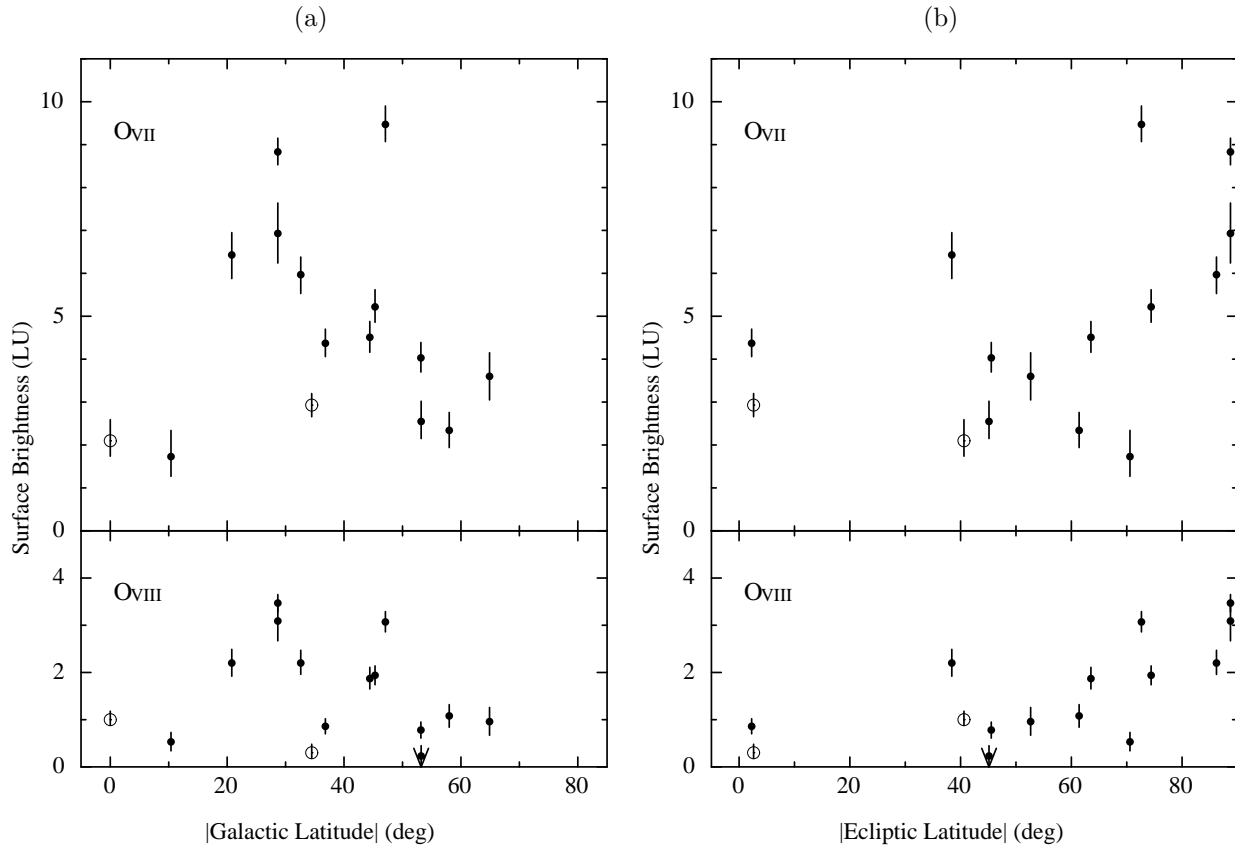


Fig. 4. OVII and OVIII emission intensities as functions of absolute Galactic latitude $|b|$ (a), and as functions of absolute ecliptic latitude (b). The two data points marked with an open circle are OVII intensities of the MBM 12 on cloud direction and the midplane direction (235, 0). Both are taken from Masui et al. (2009).

near the solar maximum in 2000-2002 and Suzaku observations near the solar minimum were noted by Koutroumpa et al. (2007) and Henley & Shelton (2008). For example, Lockman Hole $(\ell, b) = (149.1, 53.6)$ by XMM-Newton observations taken in October 2002 show much higher OVII intensities (7 to 18 LU, Koutroumpa et al. (2007)) than those of Suzaku (2.5 and 4.1 from the present LH-1 and LH-2 fields). Henley & Shelton (2008) showed that OVII line intensities on and off directions of the shadowing filament (On-FIL and Off-FIL fields) were $10.65^{+0.77}_{-0.82}$ and $13.86^{+1.58}_{-1.49}$ LU for the XMM-Newton observations in 2002 March, while they reported that the intensities were $6.51^{+0.37}_{-0.45}$ and $10.53^{+0.68}_{-0.55}$ LU for the Suzaku observations (statistically consistent with the present results, $5.2^{+1.0}_{-0.6}$ and 9.5 ± 0.7 LU). If this difference is due to the different SWCX intensity as the authors suggest, it was brighter by about 5 LU during the XMM-Newton observations. The OVII emission intensity in the MBM12 on-cloud direction determined by Chandra (1.79 ± 0.55) and Suzaku 2.93 ± 0.45 were marginally consistent within the 90 % statistical errors, although the OVIII emission intensity by Chandra (2.34 ± 0.36 LU) was larger than that of Suzaku (0.30 ± 0.20 LU).

The ROSAT sky survey was able to remove SWCX contributions with time variations on scales of a day or less, which should provide efficiencies in removing geocoronal SWCS similar to the procedures used here. The steadier

part of the heliospheric contribution is still present, however, and we might expect it to be considerably larger, since the ROSAT survey was conducted at solar maximum and the Suzaku observations near solar minimum. Both Suzaku and ROSAT are in low Earth orbit, and observing directions of the both satellites are almost perpendicular to the Sun-Earth-line.

We calculated the $R45$ band counting rate expected for the best-fit model parameters of model 1 (Table 3) and model 2 (Table 6). We used the ROSAT response function, "pspc_gain1.256.rsp", in CALDB at NASA/GSFC⁵. Two models gave consistent results within the 1σ statistical errors.

Using the database at NASA/GSFC⁶, we extracted ROSAT $R45$ band average counting rate in a circular sky region of 36 arc minute diameter centered at the Suzaku XIS aim point. The size of the sky region is larger than that of the Suzaku field of view. However, statistical precision of survey will be inadequate on smaller fields. In Figure 6, we plot the observed ROSAT counting rate as a function of expected counting rate from the Suzaku observation. In the figure we include M12on and MP235 fields using the results from Masui et al. (2009). The horizontal error bars in this figure is 1σ statistical errors

⁵ available from ftp://legacy.gsfc.nasa.gov/rosat/calib_data/pspc/cpf/matrices/

⁶ available from <http://heasarc.gsfc.nasa.gov/cgi-bin/Tools/xraybg/xraybg.pl>

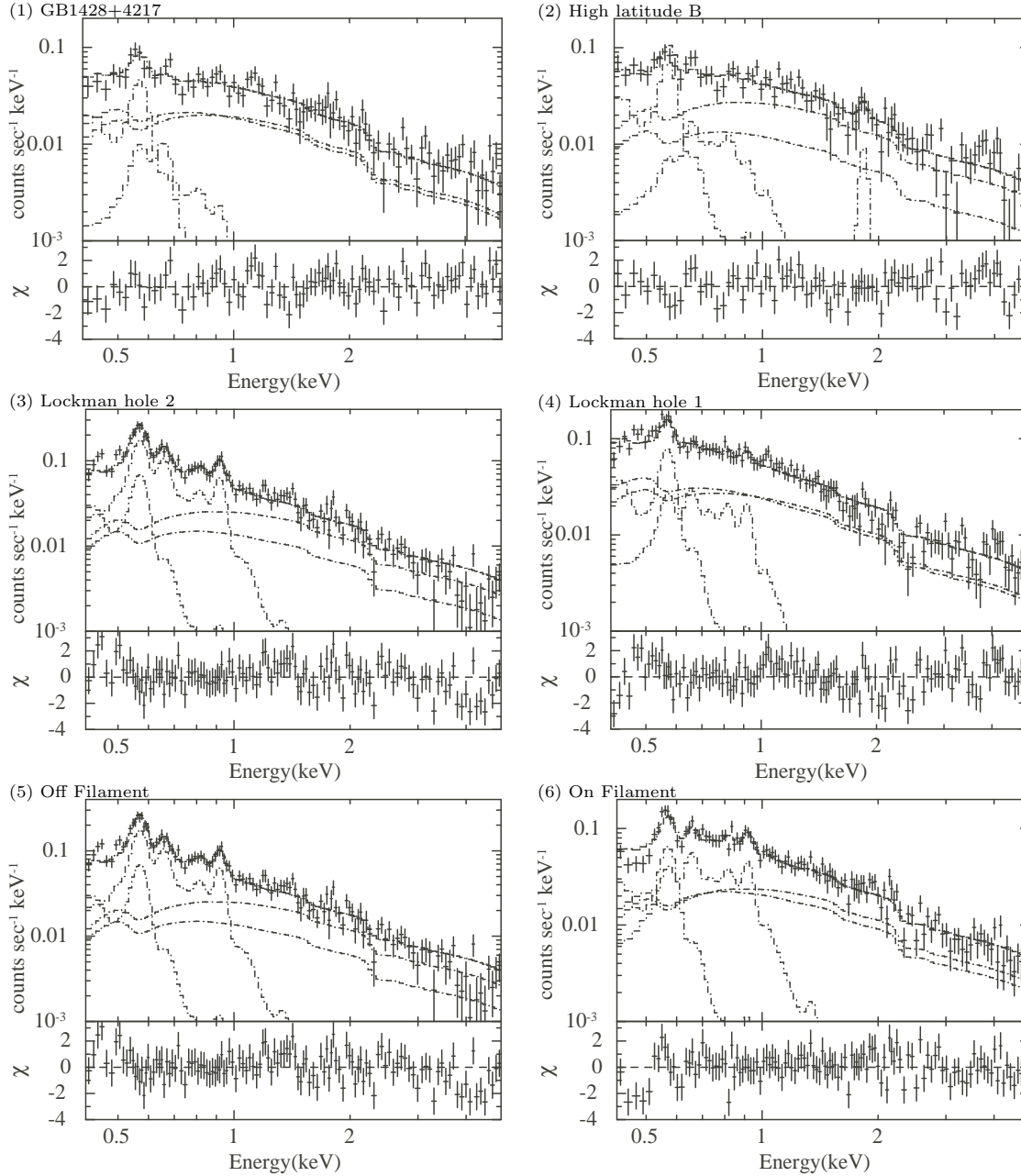


Fig. 5. Results of spectral fits with SWCX+LHB component fixed (model 2) except for MP235 (last panel). Observed spectra (crosses), best-fit model and its components (step functions) convolved with the instrument response function and residuals of the fit (bottom panels) are shown. The vertical error bars of data points correspond to the 1σ statistical errors. The model parameters of the SWCX+LHB component was taken from the midplane observation, MP235 in Table 4

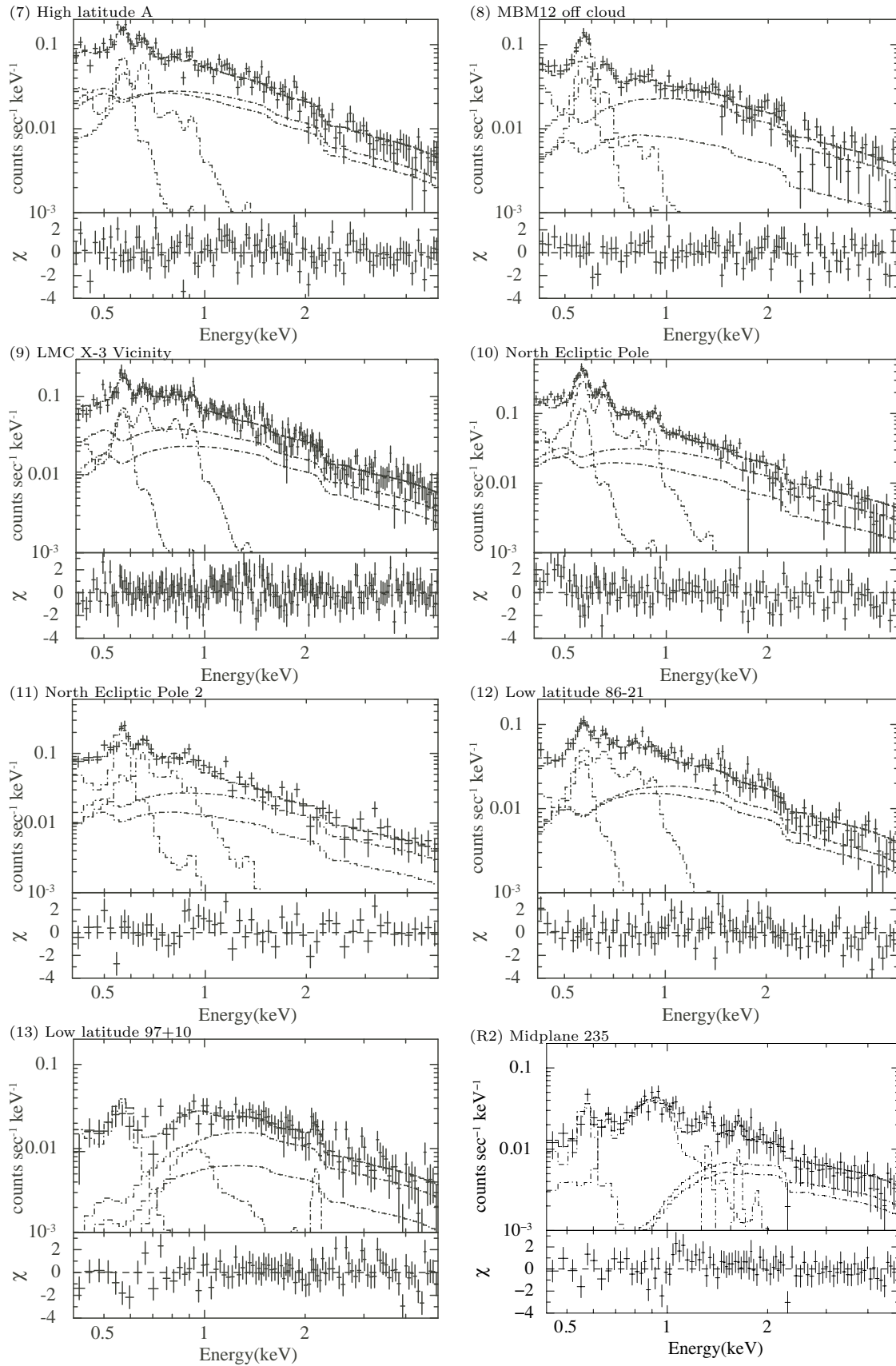


Fig. 5. Continued.

Table 8. Comparison with ROSAT all sky survey

ID	Suzaku ^a	RASS ^b <i>R45</i> band
	10^{-6} c s^{-1}	amin^{-2}
1 (GB)	85.4 ± 2.6	186 ± 21^c
2 (HL-B)	65.6 ± 2.2	150 ± 21^c
3 (LH-2)	68.4 ± 1.9	85 ± 15
4 (LH-1)	103.4 ± 2.0	103 ± 16
5 (Off-FIL)	130.4 ± 2.3	227 ± 34^c
6 (On-FIL)	105.3 ± 2.1	118 ± 27^c
7 (HL-A)	103.7 ± 2.2	112 ± 17
8 (M12off)	60.0 ± 1.8	99 ± 20
9 (LX-3)	140.0 ± 2.4	180 ± 16^c
10 (NEP1)	129.6 ± 2.4	158 ± 4
11 (NEP2)	119.8 ± 4.0	158 ± 4
12 (LL21)	109.3 ± 2.8	123 ± 14
13 (LL10)	31.6 ± 1.8	44 ± 9
R1 (M12on)	20.8 ± 0.9	37 ± 11
R2 (MP235)	58.0 ± 2.3	109 ± 21

The errors in this table are all at $1\text{-}\sigma$ significance.

^a The intensity expected in the ROSAT *R45* band from the Suzaku best-fit model function.

^b Average intensity for a circular region of $36'$ diameter centered at the Suzaku-observation aim point.

^c These directions are considered to be contaminated with the long-term enhancement: data points marked with open boxes in Figure 6.

estimated from the spectral model fits of Suzaku data: we searched for the minimum and maximum expected ROSAT counting rate for the combinations of parameters on the $\chi^2 = \chi_{\min}^2 + 1$ surface in the 5 dimensional model parameter space.

The observed and expected counting rates are well correlated. However the observed ROSAT counting rates are systematically larger than the rates expected from the present Suzaku best-fit model. The sky directions of the five data points marked with an open rectangle (GB, HL-B, Off-FIL, On-FIL, and LX-3) are on streaks of bright areas which follow the RASS scan path. We thus consider that they are possibly contaminated with the long-term enhancement, i.e. with the SWCX from the geocorona, or by the solar X-ray scattering during the ROSAT observations (Snowden et al. 1994). If we exclude these data points, the scatter of the data points from a linear relation is significantly reduced. We then fitted the relation of the remaining nine data points with a linear function: (ROSAT observed rate) = $p \times$ (rate expected from Suzaku) + q . We obtained $p = 1.08 \pm 0.12$ and $q = (16.1_{-13.6}^{+12.5}) \times 10^{-6} \text{ c s}^{-1} \text{ amin}^{-2}$. The slope p is consistent with unity within the 90% statistical errors, while the offset q is positive.

We consider that a large fraction of the positive offset can be explained by the difference in point source sensitivity of the two sets of observations. For the ROSAT map used in the present analysis, point sources with count-

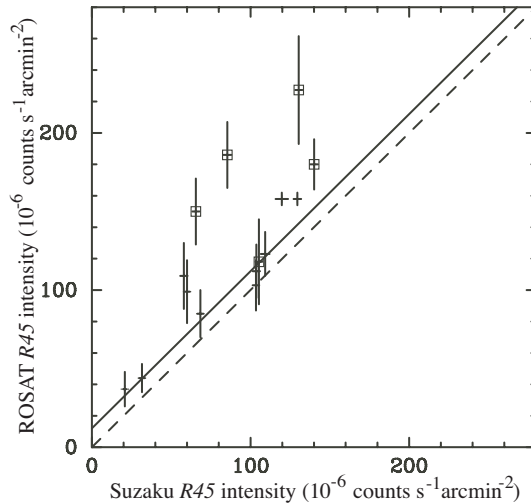


Fig. 6. Observed ROSAT *R45* band counting rate v.s. counting rate expected from Suzaku best-fit model functions. Points with open boxes are from possibly contaminated regions of the ROSAT survey. The vertical error bars are the $1\text{-}\sigma$ statistical errors of the ROSAT observation. The horizontal error bars are $1\text{-}\sigma$ statistical errors estimated from the spectral model fits of Suzaku data. The diagonal solid line shows the predicted relation including the average point source removal correction, i.e. $12 \times 10^{-6} \text{ c s}^{-1} \text{ amin}^{-2}$ above the 1:1 relation.

ing rate $> 0.020 \text{ c s}^{-1}$ in the *R45* band were removed (Snowden et al. 1997). This threshold corresponds to $3.8 \times 10^{-13} \text{ erg cm}^{-2} \text{ s}^{-1}$ in 0.47 - 1.21 keV assuming a power-law spectrum of a photon index of 1.95 and an absorption column density of $5.6 \times 10^{19} \text{ cm}^{-2}$ (see below). On the other hand, from the energy fluxes and their statistical errors of the point sources we removed from the present Suzaku analysis, we estimate the typical detection threshold for point sources to be $1 \times 10^{-14} \text{ erg cm}^{-2} \text{ s}^{-1}$ in 0.47 - 1.21 keV. Thus there is a factor of ~ 40 difference in the detection threshold. We estimated the average surface brightness of point sources in the flux range of $(1 - 38) \times 10^{-14} \text{ erg cm}^{-2} \text{ s}^{-1}$ in 0.47 - 1.21 keV, assuming the $\log N - \log S$ relations in 0.5 - 2 keV band obtained by ROSAT (Hasinger et al. 1996). To convert energy flux in 0.5 - 2 keV to the *R45* band, we assumed a broken power-law spectrum with photon indices of 1.96 and 1.4 respectively below and above 1.2 keV and various absorption column densities from $5.6 \times 10^{19} \text{ cm}^{-2}$ (Lockman hole field) to $1 \times 10^{21} \text{ cm}^{-2}$. The result we obtained was $(14 - 10) \times 10^{-6} \text{ c s}^{-1} \text{ amin}^{-2}$ in the *R45* band for $N_{\text{H}} = (0.056 - 1) \times 10^{21} \text{ cm}^{-2}$. Thus the offset q is consistent with zero if we correct for contribution of point sources in the ROSAT data. Using the average value over the N_{H} range, $12 \times 10^{-6} \text{ c s}^{-1} \text{ amin}^{-2}$, we obtain $q = (4.1_{-13.6}^{+12.5}) \times 10^{-6} \text{ c s}^{-1} \text{ amin}^{-2}$.

Although the ROSAT all sky survey was carried out near the solar maximum in 1990, the present results show that Suzaku and ROSAT *R45*-band intensities in at least nine directions were consistent with each other. The intensity of the spectral component for SWCX+LHB in

model 2, which contains OVII emission of 2.1 LU produces a ROSAT *R45* counting rate of $14 \times 10^{-6} \text{ c s}^{-1} \text{ amin}^{-2}$. Since this is comparable to the 90 % confidence upper limit of the offset q ($= 17 \times 10^{-6} \text{ c s}^{-1} \text{ amin}^{-2}$), it suggests that on average, the maximum increase in heliospheric OVII emission intensity between the ROSAT and Suzaku is at most ~ 2 LU, or a factor of two. Since the solar maximum increase should include lines from higher ionizations states such as OVIII and NeIX that are more efficient in producing *R45* counts, the increase in OVII is probably much less than this.

In section 2.3, we tried to remove as much as possible the time intervals in which the X-ray spectrum was contaminated by the SWCX from the geocorona. Consistency between the ROSAT and Suzaku data also indicates successful removal.

4.2. Intensity variations and temperature of the TAE

Although the solar wind has a broadly simple structure, with the slow wind confined to low ecliptic latitudes during solar minimum, the spatially non-uniform distribution of neutral H and He around the Sun leads to a complex pattern of SWCX emissivity. The distribution on the sky of *observed* SWCX emission is also a function of the observer's particular viewing geometry, as noted for example by Lallement (2004) and Robertson & Cravens (2003), requiring detailed modeling which is beyond the scope of this paper. The general level of SWCX emission in the *R45* band, however, is expected to be too small to explain the spatial variations observed in our work, consistent with our interpretation in model 2 that the spatially dependent components of OVII emission are associated primarily with the TAE component and not with SWCX.

Yao et al. (2009) constructed a thick hot disk model extending above the Galactic disk in order to simultaneously explain the absorption and emission lines observed in the energy spectra of LMC X-3, the X-ray binary in the LMC, with Chandra, and in the energy spectra of the X-ray diffuse emission in the two directions about $30'$ away from LMC X-3 observed with Suzaku. They assumed density and temperature distributions exponentially decreasing in the direction perpendicular to the Galactic disk. They obtained as the best-fit parameters the scale heights of $h_T \xi = 1.4(0.2, 5.2)$ kpc and $h_n \xi = 2.8(1.0, 6.4)$ kpc for temperature and density respectively, and the midplane gas temperature and H ion density of $T_0 = 3.6(2.9, 4.7) \times 10^6$ K and $n_0 = 1.4(0.3, 3.4) \times 10^{-3} \text{ cm}^{-3}$, where ξ is the filling factor of the hot gas. The emission-measure weighted average temperature along a line of sight is $T_0/(1 + h_n/(2h_T)) \sim 0.16$ keV. This is lower than the best-fit temperatures of the TAE component with model 2 Table 6, although the discrepancy is not very large taking the errors in T_0 and h_n/h_T into account.

For a plane-parallel configuration, we expect the intensity of the emission to increase from high to low latitude as $\propto \sin^{-1} |b|$, with a rapid decrease at low latitudes, $b \lesssim 10^\circ$, due to Galactic absorption with a much smaller scale height than the emission. In Figure 7, in-

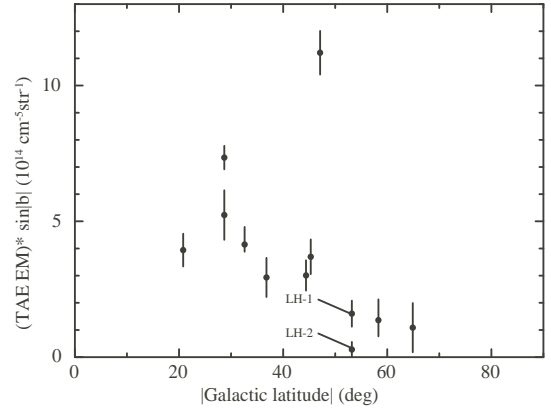


Fig. 7. The emission measure of the TAE component multiplied by $\sin |b|$ as a function of $|b|$. The TAE normalization factors are taken from model 2 (Table 6). The data point LL10 is not plotted because the higher temperature component of this field is like to have a different origin from other fields.

stead of OVII emission intensity, we show the emission measure of the TAE component for model 2 multiplied by $\sin |b|$ ($EM \sin |b|$). $EM \sin |b|$ shows a large direction-to-direction fluctuation from a constant, which suggests that the hot gas is patchy and consists of number of blobs. The short angular scale spatial variation between the two Lockmann hole fields, LH-1 and LH-2, is puzzling. These are separated by only 0.42° , but the TAE component and OVII emission are significantly stronger for LH-1 (Table 7, 5). The ROSAT map also show a difference in *R45* intensities of the two fields (Table 8), although the field of view of the two ROSAT fields are overlapped. Since the distance between two lines of sight is only 10 pc at 1 kpc away from the sun, the density contrast of hot plasma must be high between outside and inside the blobs. Figure 7 may also indicate that $EM \sin |b|$ is systematically larger for $|b| \lesssim 50^\circ$, than for $|b| \gtrsim 50^\circ$. However, this could be a chance effect, and we need more data points, in particular for $|b| \gtrsim 50^\circ$.

We estimate the parameters of hot gas by assuming an isotropic temperature of $kT = 0.222$ keV for simplicity. The total luminosity of the emission is estimated from the average value of $EM \sin |b|$, assuming a plane parallel density distribution as

$$L = 8\pi^2 \Lambda(T) \overline{EM \sin |b|} R^2,$$

where $\Lambda(T)$ and R are, respectively, the emissivity per emission measure at a temperature T , and the outer cylindrical radius of the emission region. Using the values of $\Lambda(T)$ for bolometric flux (Sutherland & Dopita 1993) and 0.3-2 keV band (APEC), we obtain,

$$L_{\text{bol}} = 3.8 \times 10^{39} \text{ erg s}^{-1} \times \left(\frac{\overline{EM \sin |b|}}{3.6 \times 10^{14} \text{ cm}^{-5} \text{ str}^{-1}} \right) \left(\frac{R}{15 \text{ kpc}} \right)^2,$$

$$L_{0.3-2\text{keV}} = 1.1 \times 10^{39} \text{ erg s}^{-1}$$

$$\times \left(\frac{\overline{EM \sin |b|}}{3.6 \times 10^{14} \text{ cm}^{-5} \text{ str}^{-1}} \right) \left(\frac{R}{15 \text{ kpc}} \right)^2,$$

The midplane density and the total mass of the hot gas, M_{tot} , can be estimated by further assuming the scale height.

$$n_0 = 1.3 \times 10^{-3} \text{ cm}^{-3} \times \left(\frac{\overline{EM \sin |b|}}{3.6 \times 10^{14} \text{ cm}^{-5} \text{ str}^{-1}} \right)^{1/2} \left(\frac{h\xi}{1.4 \text{ kpc}} \right)^{-1/2},$$

and

$$M_{\text{tot}} = 6.5 \times 10^7 M_{\odot} \left(\frac{\overline{EM \sin |b|}}{3.6 \times 10^{14} \text{ cm}^{-5} \text{ str}^{-1}} \right)^{1/2} \times \left(\frac{R}{15 \text{ kpc}} \right)^2 \left(\frac{h\xi}{1.4 \text{ kpc}} \right)^{1/2}.$$

As the scale height, h , of hot gas we assumed the temperature scale height from Yao et al. (2009), since it is smaller than the density scale height.

Yao et al. (2009) concluded that the plasma responsible for the OVII and OVIII absorption and emission towards LMC X-3 cannot be isothermal. However, the temperatures averaged over line of sight for various directions determined by OVII to OVIII ratio was remarkably constant (Figure 3). A possible origin of the hot gas is supernovae. In fact both the total mass and the total thermal energy of the hot plasma can be supplied at a supernova rate of 10^{-2} y^{-1} within the radiative cooling time of 3 Gy. However, there is no particular reason why the gas should prefer $kT = 0.2 \text{ keV}$. The spectra of the halo emission of nearby star-forming galaxies and of some of normal galaxies are described by two-temperature models with kT 's in the range of 0.1 to 0.8 keV (Strickland et al. 2004; Tüllman et al. 2006; Yamasaki et al. 2009). Thus we consider that $kT = 0.2 \text{ keV}$ is specific for our Galaxy. Then it is likely related to the virial temperature ($kT = 0.2 \text{ keV}$) for the rotation velocity of 200 km s^{-1} (e.g. Kereš et al. (2005)). A possible explanation for this coincidence is that the hot gas was formed by cosmological accretion (Tfot et al. 2002; Rasmussen et al. 2009). The total luminosity of our Galaxy estimated above is consistent with the simulations. However, the radiative cooling time of the hot gas is 3Gy, and the hot gas needs to be supplied at least on this time scale. Another interpretation is also possible that higher temperature gas has escaped from the potential and that the gas at the temperature near the virial temperature remains, since the escape time scale is by a factor of five shorter than the radiative cooling time scale.

From the spectral fits with model 2, we obtained 2 to 3 solar for [Ne/O] and [Fe/O] abundance ratios for four of the spectra. However, in model 3 (Table 7), we showed that these Fe-L and Ne "excess" emission can be explained by a higher temperature components of $kT = 0.5 - 0.9 \text{ keV}$. The HL-B field shows a high O emission temperature (0.30 keV, see Figure 3 and Table 6). Since all these fields

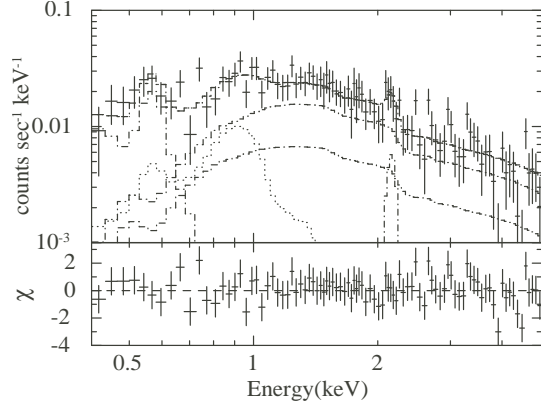


Fig. 8. Fit result of the Low Latitude 97+10 (data ID 13) spectrum using the faint dM star model by Masui et al. (2009) instead of the TAE component.

are in high ecliptic latitudes, where only low-ionization-temperature winds are emitted from the sun during solar minimum, the Heliospheric SWCX is not likely origin of the excess Ne and Fe emission. These lines of sight may contain blobs of high ($> 0.22 \text{ keV}$) temperature hot gas which may be on the way to escape from our Galaxy.

4.3. The spectrum of the $b = 10^\circ$ sample

We obtained significantly higher temperature (0.75 keV) for the TAE component for Low Latitude 97+10 (LL10) than that of other samples (average = 0.2 keV). This direction has a high Galactic absorption of $2.78 \times 10^{21} \text{ cm}^{-2}$, and the transmissions for OVII and OVIII are respectively only about 10 and 20 %. Thus the emission from the thick disk of temperature $\sim 0.2 \text{ keV}$ will be significantly absorbed and hard to detect, if it exists in this direction. Masui et al. (2009) detected an emission component of the similar temperature in the energy spectrum of the midplane direction, MP235. They suggested that the component is a sum of emission from unresolved faint dM stars existing between the bulk of Galactic absorption and the Earth, and constructed model spectra assuming an average dM star spectrum with two-temperature thermal emission, the stellar X-ray luminosity distribution functions, and the spatial densities of dM stars in the literature. The model spectrum could consistently explain the observed spectrum not only in spectral shape but also in absolute intensity within 30 %. We fitted the LL10 spectrum using their dM star model spectrum constructed for $(\ell, b) = (90^\circ, 10^\circ)$, instead of the TAE component in model 1. As shown in Figure 8, this model reproduces the observed spectrum well ($\chi^2 = 89.2$ for 90 degrees of freedom). However, it was necessary to increase the intensity of the emission by a factor of about 5 from the model. This suggests that the emission from dM stars does not decrease so rapidly with increasing b as the model predicts, or that there are large spatial fluctuations at $b \sim 10^\circ$. We need more observations at low Galactic latitude in order to solve this problem.

5. Summary

We presented spectra of soft diffuse X-ray emission in twelve fields observed with Suzaku together with the spectra of two other fields analyzed by Masui et al. (2009). In the data reduction, we carefully removed the contributions of the solar-wind charge-exchange (SWCX) induced X-ray emission from the geocorona. However, ~ 1.5 LU uncertainty remains in OVII intensity. The discrepancy between the two NEP observations (1.9 LU) can be partly due to yet incomplete removal of geocoronal SWCX.

To determine O emission intensities, we first fitted the spectra with a model consisting of a broken power-law component for the CXB, and two thin thermal emission components of the solar abundance, one of which are subject to Galactic absorption (model 1). The OVII and OVIII emission intensities were determined using the model by setting O abundances of two thermal emission components to zero and adding two Gaussian functions to represent OVII and OVIII. The OVII and OVIII intensities are strongly correlated and suggest the existence of an intensity floor for OVII emission at ~ 2 photons $\text{s}^{-1} \text{cm}^{-2} \text{str}^{-1}$ (LU). The OVIII emission intensity of nine high-latitude fields show a tight correlation with the excess of the OVII intensity above the floor. The relation is approximated as $(\text{OVIII intensity}) = 0.5 \times [(\text{OVII intensity}) - 2 \text{ LU}]$. These suggest that the OVII emission arises from two origins: approximately uniform emission of about 2 LU, and spatially variable (0-7 LU) emission from hot plasma of a temperature of ~ 2 keV. The former is likely to arise from Heliospheric Solar Wind Charge Exchange plus the local hot bubble (SWCX+LHB), and the latter from hot gas in more distant parts of the Galaxy, i.e. the transabsorption emission (TAE). It is remarkable that for most of the fields, TAE average emission temperatures are confined in a narrow range ($\sim \pm 0.2$ keV) around 0.2 keV. This temperature may be related to the virial temperature of the Galaxy, which locally corresponds to the rotation velocity of $\sim 200 \text{ km s}^{-1}$.

The O emission intensities of the two thermal components of model 1 do not reproduce the above characteristics of O emission. This is because the abundance is fixed to the solar, while strong Ne and Fe-L emissions exist in some of the spectra. The observed spectra can be fitted with a model in which the intensity and temperature of the non-absorbed SWCX+LHB component are fixed to nominal values if we set the Ne and Fe abundances of absorbed TAE component free (model 2), or if we include an additional higher temperature component (model 3). We found that four spectra required Ne to O abundances as large as 3 solar with model 2. Alternatively, these spectra can be fitted by model 3 with a higher temperature (0.5 - 0.9 keV) emission component with solar abundances. The temperatures of the TAE component obtained with these two models were consistent with the values expected from the OVII to OVIII ratio.

The surface brightnesses estimated from the present best-fit model function were statistically consistent with the ROSAT All Sky Survey (RASS) map, even though

the present observations were performed during solar minimum, while the RASS was in solar maximum. The upper limit for the difference was estimated to be $17 \times 10^{-6} \text{ c s}^{-1} \text{ amin}^{-2}$ *R45*-band counting rate after corrected for the difference in point source removal threshold between the present Suzaku observations and the RASS.

The origin of the TAE component was discussed in the context of the thick hot disk constructed by Yao et al. (2009). The emission measure determined by model 2 shows a large deviation from the $\sin^{-1} |b|$ dependence expected from a plane parallel configuration, which we consider to suggest short spatial scale structure of the hot gas. The total luminosity, midplane density, and the total mass of the hot gas were estimated assuming simple cylindrical geometry and a uniform temperature. The canonical temperature of the TAE component, $kT \sim 0.2$ keV, may be related to the virial temperature of our Galaxy.

The lowest latitude sample of the present analysis, $b = 10^\circ$, contains emission with $kT = 0.75$ keV instead of 0.2 keV. The spectral shape of this component can be represented by the faint dM star model by Masui et al. (2009). However the intensity must be increased by a factor of about five from the model.

The authors are grateful to the anonymous referee for his comprehensive comments and useful suggestions, which improved the paper very much. They also would like to thank the Suzaku team for their effort for the operation of the spacecraft, the calibration of the instruments, and the data processing.

References

- Anders E. & Grevesse N. 1989, *Geochimica et Cosmochimica Acta* 53, 197
- Cox, D.P. 1998, *Lecture Notes in Physics* (Berling: Springer Verlag), 506, 121
- Cox, D.P. 2005, *ARA&A*, 43, 337
- Cravens, T.E.. 2000, *ApJ*, 532, L153
- Cravens, T.E.. 2000, Robertson, I.P., & Snowden, S.L. J. *Geophys. Res.*, 106, 24883
- Dickey, J.M. & Lockman, F.J. 1990, *ARA&A*, 28, 215
- Ferrière, K.M. 2001, *Rev. of Mod. Phys.*, 73, 1031
- Fujimoto, R. et al. 2007, *PASJ*, 59, S133
- Galeazzi, M. et al. 2007, *ApJ*, 658, 1081
- Hasinger, G. et. al 1993, *A&A*, 275, 1
- Henley, D.B. et al. 2007, *ApJ*, 661, 304
- Henley, D.B. & Shelton, R.L. 2008, *ApJ*, 676, 335
- Ishisaki, K. et al. 2007, *PASJ*, 59, S53
- Kereš, D. et al. 2005, *MNRAS*, 363, 2
- Kharchenko, V., Rigazio, M., Dalgarno, A., & Krasnopolsky, V. A. 2003, *ApJL*, 585, L73
- Koutroumpa, D. et al. 2006, *A&A*, 460, 289
- Koutroumpa, D. et al. 2007, *A&A*, 475, 901
- Koutroumpa, D. et al. 2008, in proceedings of ‘From the Outer Heliosphere to the Local Bubble’, ISSI workshop, Bern October 2007 (arXiv:0805.3212)
- Koyama et al. 2007, *PASJ*, 59, S23
- Kuntz, K.D. & Snowden, S.L. 2000, *ApJ*, 543, 195
- Kuntz, K.D. & Snowden, S.L. 2008, *ApJ*, 674, 209
- Lallement, R. 2004, *A&A*, 418, 143

- Masui, K. et al. 2009, PASJ, 61, S115
McCammon, D. & Sanders, W. 1990, ARA&A, 28, 657
McCammon, D. et al. 2002, ApJ, 578, 188
Miller, E.D. et al. 2008, PASJ, 60, S95
Mitsuda, K. et al. 2007, PASJ, 59, S1
Mitsuda, K. et al. 2008, Prog. of Theor. Phys. Suppl, 169, 79
Rasmussen, J. et al. 2009, ApJ, 697, 79
Robertson, I. P. & Cravens, T. E, 2003, J. Geophys. Res., 108,
LIS 6-1
Serlemitsos, P.J. et al. 2007, PASJ, 59, S9
Smith, R.K. et al. 2007, PASJ, 59, S141
Smith, R.K. et al. 2005, ApJ, 623, 225
Snowden, S.L. et al. 1994, ApJ, 424, 714
Snowden, S. L. et al. 199), ApJ, 485, 125
Snowden, S. L. et al. 2000, ApJS, 128, 171
Strickland, D.K. et al. 2004, ApJS, 151, 193
Sutherland, R.S. & Dopita, M.A. 1993, ApJS, 88, 253
Tawa et al. 2008, PASJ, 60, S11
Tfot, S. et al. 2002, MNRAS, 335, 799
Tüllman et al. 2006, A&A, 448, 43
Tsyganenko, N.A. & Sitnov M.I. 2005, J. Geophys. Res., 110,
A03208
Yao, Y. & Wang, Q.D. 2008, ApJ, 658, 1088
Yao, Y. et al. 2009, ApJ, 690, 143
Yamasaki N.Y. et al. 2009, PASJ, 61, S291